Abstract

Kim, Chang Hyeuk. A study of an area x-ray source for Diffraction Enhanced Imaging for Clinical and Industrial Applications. (Under the Direction of Professor Mohamed A. Bourham.)

Research in diffraction-enhanced imaging (DEI) has shown strong potential in obtaining high-resolution images as compared to conventional radiographs. A successful development of a compact size DEI system would greatly improve x-ray diagnostics in the medical field, as well as potential application in material science research and other industrial applications.

DEI experimental research, using a synchrotron source, has shown success and proven to be an attractive medical diagnostics method. While the use of a synchrotron source might be applicable, however, a clinical system would rather use an x-ray source that could be integrated into a radiology system feasible for hospital and clinical practices.

This research is aiming to develop an area x-ray source that replaces the need for a synchrotron source by providing a monochromatic area x-ray beam collimated over 100cm^2 area. Reasonable operation time (5-10 sec) is also a desirable feature with efficient thermal management of the x-ray tube (target and housing). The x-ray flux should be comparable to synchrotron source flux (1.4×10^{12} photon/mm^2/sec). The peak power must not exceed 200kW for feasible use in a major medical facility or industrial complex. A computational study of concentric filament area x-ray source has been investigated in this research.

The design features are based on generating electrons from three concentric circular filaments to provide an area electron flux, with a 60kV accelerating potential. The x-ray target is a grounded stationary oxygen-free copper target with a layer of molybdenum

(manufactured by BranXray Co., Inc.). Study of electron trajectories and their distribution at various tilt angles of the target was completed using the SIMION 3D code. Heat loading and thermal management is studied using an in-house developed thermal and heat transfer code. X-ray flux and energy distribution for aluminum and beryllium windows was studied using MCNP 4C2 Monte Carlo code. A prototype area x-ray source, a proof-of-principle device, is under construction in the Department of Nuclear Engineering, NCSU to investigate the feasibility of area x-ray generation and the scalability to clinical and industrial aspects. Other researchers will use the computational results of this thesis as a predicting tool to determine and optimize the prototype device operational parameters, and to benchmark the experimental results.

A study of an areas x-ray source for Diffraction Enhanced Imaging for Clinical and Industrial Applications

By

Chang Hyeuk Kim

A thesis submitted to the Graduate Faculty of
North Carolina State University
in partial fulfillment of the
requirements for the Degree of
Master of Science

Department of Nuclear Engineering
North Carolina State University
Raleigh, North Carolina

2004

APPROVED BY:

Dr. Mohamed A. Bourham, Chair	**Dr. J. Michael Doster**
Dr. Dale E. Sayers	**Dr. Marian G. McCord**

Biography

Chang Hyeuk Kim was born May 22, 1976 in Gwangju, South Korea. He grew up within Gwangju with his parents, Woo-Jeon Kim and Kyoung-Sook Beck, as well as his sister, Nu-Lee Kim. After he graduated from Gwangju Insung high school, he started college education at Chosun University as a Nuclear Engineering student in 1994. He joined military service for two and half years, in the Korean Air Force in 1995. He returned to school in 1998. After obtaining his BS degree in 2002, he joined the graduate program at North Carolina State University working on his MS degree. He married his classmate Su-Jin Oh in June, 2003.

Acknowledgement

I would like to express my gratitude to Dr. Mohamed A. Bourham. He has been my academic advisor and good example to me as a researcher. Without his kindly and sincere guidance, I could not complete this thesis. I am also grateful to my committee members, Dr. Doster, Dr. Sayers, and Dr. McCord for their comments on my thesis. Dr. Doster helped me in the thermal analysis and running his code. I must also acknowledge the Nuclear Engineering department and faculty, without this department's financial support I could not have performed this research at North Carolina State University. I also would like to express my thanks to Dr. Man-Sung Yim for his invaluable guidance during the course of my master's program studies.

Table of Contents

page

List of Figures

page

List of Tables

page

Chapter 1

Introduction

Recent research in medical imaging has provided various means by which high resolution images could be obtained. The various imaging techniques have different capabilities, and some have progressed dramatically during past fifty years. X-ray imaging, radiology, although it is one of the oldest techniques (Roentgen 1895), has proven to be one of the standard reliable radiology methods. Recent research in diffraction-enhanced imaging (DEI) has shown strong potential in obtaining high-resolution images over other known technique [1]. Images obtained using DEI, with the utilization of a synchrotron beam, have shown the benefits of DEI over other x-ray radiology and other imaging system. However, the use of a synchrotron source necessitates having a DEI system close to a major synchrotron facility. The synchrotron source provides a monochromatic highly collimated beam, which is necessary for diffraction-enhanced imaging. A clinically approved DEI system, which may be installed in major hospitals, would need a new x-ray source that can provide a substitute for a synchrotron source. Although medical imaging may appear as the primary application of DEI, but the application extends to material science research and various industrial applications such as advanced radiography for cargo and parcel screening with enhanced resolution for active interrogation techniques.

Diffraction Enhanced Imaging (DEI) was developed and reported by Chapman, et al. [1]. The images obtained from their DEI system have much better contrast and high resolution as compared to conventional radiographs. Their experimental DEI system has used a highly collimated synchrotron radiation source, from the X15A beam line at the National Synchrotron Light Source of Brookhaven National Laboratory. The system employed two different types of crystals for producing monochromatic and diffracted x-ray beams. This system is completely free of scattering and the beam contains only the contribution from x-rays that are affected by absorption, extinction or refraction through a very small angular deflection of the order of microradians (5.73×10^{-5} degree/microradian). This arrangement made it possible to obtain higher contrast images from the same object.

The purpose of this study is to investigate the feasibility of developing a new compact size area x-ray source capable of producing typical parameters needed for diffraction-enhanced imaging without using a synchrotron source. This computational study would be used as the proof-of-principle towards developing a clinically approved DEI system for medical radiology, and scalability to other industrial applications including active interrogation of cargo and parcels. The desirable features of an area x-ray generator are:

- Peak electric power less than 200 kW
- High x-rays flux ($\sim 10^{12}$ ph/mm^2/sec)
- Output x-ray beam collimated over a 100 cm^2 area
- Reasonable operation time (~ 5 – 10 seconds)
- Stationary (non-rotating) target assembly and concentric or spiral filament configuration.

This research is a computational study of the design aspects of an area x-ray source to be used as a predicting tool for optimization and scalability to the engineering of an actual industrial system. The major design aspects of this study are the electrostatic analysis and electron trajectories and their distribution, the thermal analysis and target heat loading for appropriate operation time, and investigation of x-ray energies and x-ray flux at the extraction window of the system. Computational studies were performed using three computer codes, SIMION 3D, 2-Dimentional heat transfer code, and MCNP 4C2.

Chapter 2

Background

2.1 Typical X-ray imaging method

X-ray radiography is one of basic diagnostics in medical imaging. It is based on the attenuation of an x-ray as it travels through a medium, and the specific density of the medium and the energy of the incident beam determine the attenuation coefficient. A medium with a structure of different compositions will attenuate the incoming beam with different attenuations. A detector, or x-ray film, will thus indicate the structure of the medium. For human body, the concept is the same and a radiograph is a picture obtained due to different attenuation in the human body for a given exposure rate on the film or the detector [3]. A basic radiography system has an x-ray generator on one side of the patient, and an x-ray detector on the other side. When X-ray travels through the body, the attenuation is different in different tissue or bones due to their difference in attenuation coefficients. The film, or x-ray detector, will detect the difference in x-ray intensities after attenuation through the medium. The contrasts on the film or amplitudes on a digital detector produce an image of the structure of the medium. Radiographic images in the medical practice are widely used to obtain images of broken bones, kidney stones, lung cancer, cardiovascular disorder, etc. [3]. Mammography is one of the radiography methods to diagnose breast cancer. It uses much lower x-ray energies than other radiography applications, because the linear attenuation coefficients of normal and cancerous tissue in the breast have little difference at the lower x-ray energy levels. The linear attenuation coefficients of breast tissue and tissue-equivalent materials [4] are shown in Figure 2-1.

The different attenuation coefficients of these tissues are not detectable with conventional radiography devices, which use relatively high-energy x-ray. The spectrum of a conventional x-ray tube [5] is shown in Figure 2-2. The images from these energy ranges cannot efficiently discriminate between normal and cancerous breast tissues. As a corollary, modern mammography systems have x-ray sources and detector systems specifically designed for breast imaging.

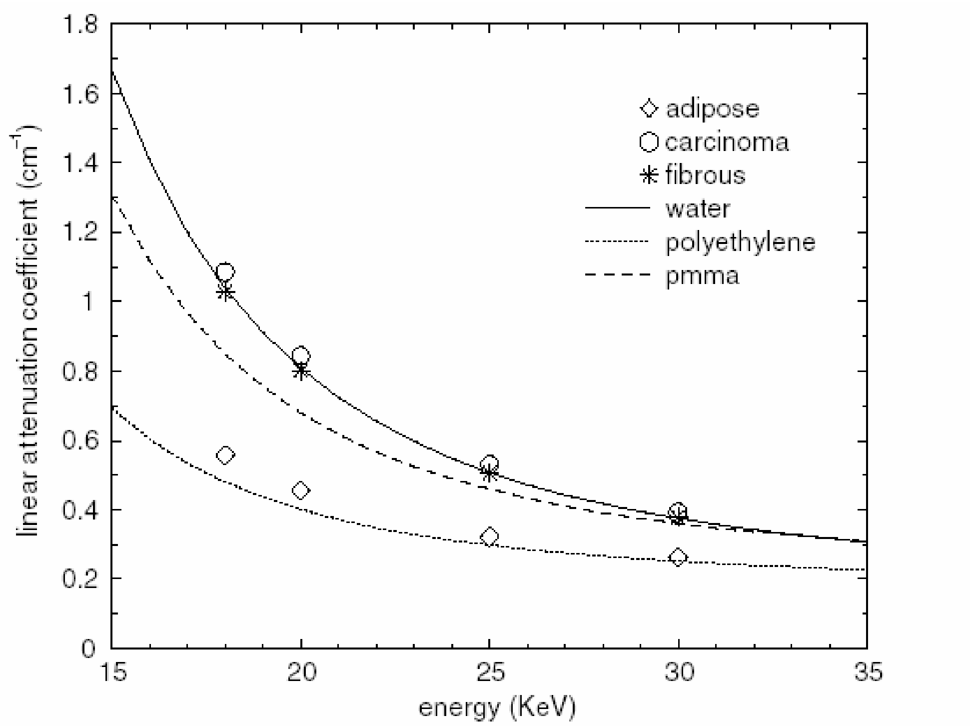

Figure 2- 1 Linear attenuation coefficients for breast tissue and tissue-equivalent material (Ref.: A Taibi, et al 2003)

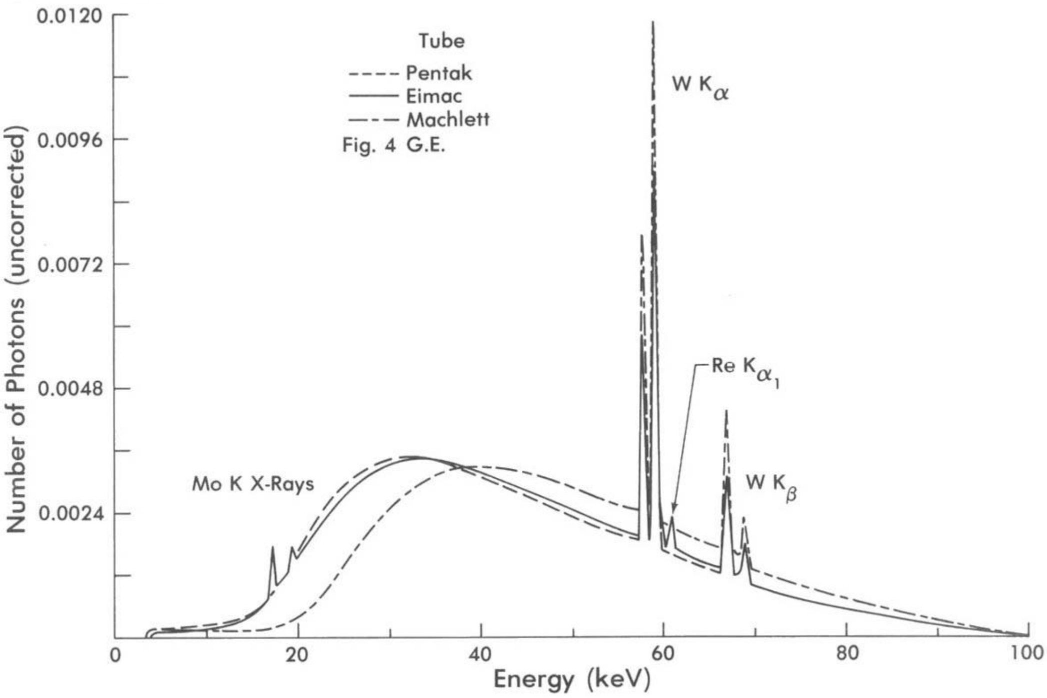

Figure 2- 2 The conventional x-ray tube spectrum (Ref.: FDA 81-8162, 1981)

2.2 Diffraction-Enhanced Imaging

2.2.1 Principle of DEI

Conventional x-ray radiography uses an x-ray beam to penetrate an object, and the attenuation of x-ray occurs through the structure of the object resulting in different attenuated intensities. The difference in attenuation results in a spatial distribution of the attenuated x-rays on the film or the digital detector. However, x-ray attenuation process is not only due to interaction between the incident x-rays and an object, it included absorption, refraction and scattering. The scattering many include small angle, which is less than milliradians. Scattered beam contains information on the structure of the object, and such information is not obtainable in conventional radiography systems.

Figure 2-3 illustrates the synchrotron setup used to obtain radiographs of an object and the addition of the analyzer crystal (Bragg or reflection geometry) used to implement the DEI system at the synchrotron (D. Chapman et al., 1997; [1]). In the shown setups, a Si(333) double crystal monochromator is used to select required x-ray energy range for the synchrotron beam, while for the DEI Bragg case setup the Si(333) crystal serves as the Bragg analyzer. As previously mentioned, information from x-ray scattering and diffraction are lost in conventional radiography. In diffraction-enhanced imaging DEI Bragg setup, with Si(333) Bragg analyzer, it allows for such information to be obtained [6].

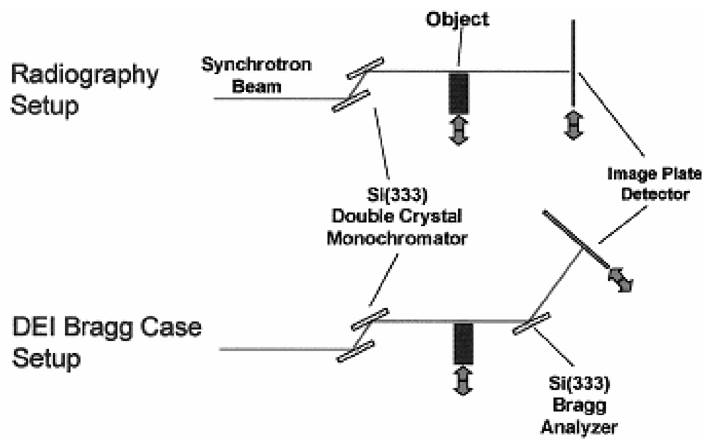

Figure 2- 3 A DEI Bragg and a radiography setup (Ref.: D. Chapman. 1997)

It is important to mention that in both set ups of Figure 2-3, a Si (333) double crystal monochromator is used, but the addition of a Si (333) Bragg analyzer is necessary for the DEI Bragg setup. To further clarify this necessity, for DEI imaging, the imaging beam is generated by diffracting the polyenergetic synchrotron to create a near monoenergetic imaging beam. The imaging beam passes through the object as in conventional radiography but a matching crystal (Bragg analyzer) is placed between the object and the detector, and is set at or near the peak of the Bragg diffraction angle. The condition for diffraction from the Bragg analyzer limits the x-rays that can be diffracted into the detector and thus provides a high degree of scatter rejection, which results in obtaining an improved image contrast. The Bragg analyzer provides almost complete scatter rejection due to the fact that the analyzer only accepts narrow angles in the range of few microradians. The Bragg analyzer provides the tools necessary to prepare and analyze x-ray beams traversing an object on the microradian scale [7], and thus this Bragg analyzer is a necessity for a DEI setup. The material of the crystal is typically silicon. The purity and perfection of these crystals have allowed many advances in x-ray diffraction techniques and in particular at synchrotron x-ray sources. The condition for x-ray diffraction from a crystal is met only when the incident beam makes the correct angle to the atomic lattice planes in the crystal for a given x-ray energy, or wavelength. When this condition is met, the beam diffracts from the planes over a narrow range of incident angles, which is called the Bragg diffraction. As the crystal is rotated around the axis parallel to the lattice plane and perpendicular to the incident beam direction, the intensity variation is referred as the rocking curve. The shape of this curve is roughly triangular with the peak reflectivity approaching near 100%.

The intensity of x-ray, after penetrated an object in normal radiography, can be expressed by:

$$I_N = I_R + I_D + I_C + I_I$$

where, I_N is the source of contrast at the detector plane. The portions of coherent scattering and incoherent scattering are I_C and I_I, respectively; and the diffraction intensity is given by I_D, which arrives on the detector along with the portion of incident beam I_R that has been affected by refraction and attenuated by absorption or extinction.

In a DEI system, the portion of refracted beam I_R will be separated from the other components and shows contrast based on refraction, absorption, and extinction. The scattering component, I_C and I_I, contribute to loss of contrast and spatial resolution, which can be improved by using a synchrotron source and a monochromator. Synchrotron radiation offers high intensity and good natural collimation of the radiation. The characteristics of synchrotron radiation make it possible to select a narrow wavelength by a crystal monochromator [8]. In addition, the crystal diffraction optics could also be used to eliminate coherent and incoherent fractions I_C and I_I, respectively. The crystal analyzer diffracts the x-ray, which is aligned within the angular acceptance (rocking curve), onto the detector. It is possible to remove the scatter contribution to the image. The width of the rocking curve is few microradians. After eliminating the coherent I_C and the incoherent I_I scattering portions, the incident beam has only the refracted portion I_R, which is very close to the initial direction.

In the DEI setup, two images are obtained depending on the position on the rocking curve. One image is the apparent absorption image, which is an actual image from direct transmission. The other is the refraction image, which is correlated to the gradient of the refractive index along the path of the x-ray through the object. To facilitate this, an example of two images of an object are obtained; one through an analyzer angle that is slightly greater than the peak angle of the rocking curve (higher side image), and one at lower than the peak angle (lower side image). The rocking curve and two DEI images are shown in Figure 2-4 [1].

The analyzer crystal diffracts the beam in the vertical plane. Therefore, the sensitivity of x-ray diffraction is only to vertical component $\Delta\theta_Z$.

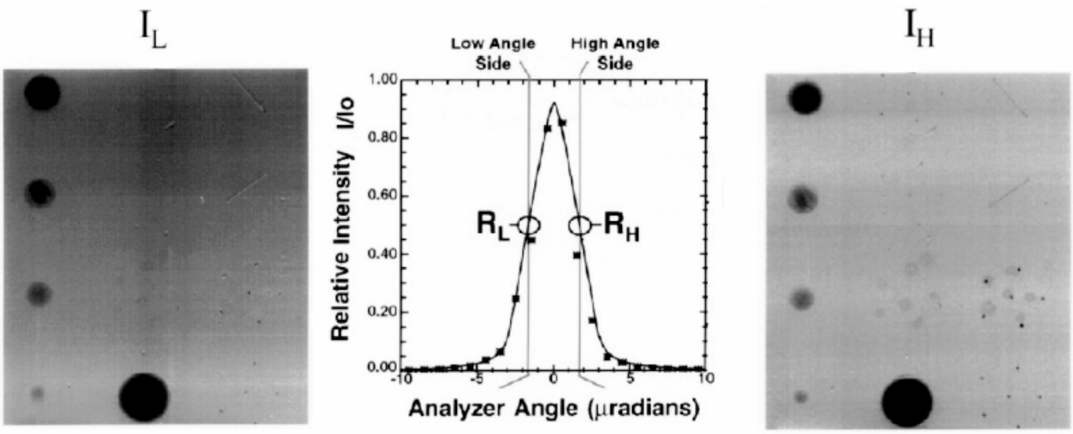

Figure 2- 4 The rocking curve and examples of higher an lower side images (Ref.: D. Chapman, 1997)

According to Chapman, et al [1], the intensity diffracted by the analyzer is set as a relative angle θ_i from the Bragg angle θ_B where θ_B+ θ_i is the angle between the incident beam and diffraction planes and is given by

$$I_i = I_R R(\theta_B \pm \theta_i)$$

where I_i is the intensity at relative angle θ_i from Bragg angle θ_B, I_R is defined as the portion of the incident beam which has only been affected by refraction and attenuation by absorption and extinction, and $R(\theta)$ is the analyzer reflectivity function at angle θ. The analyzer reflectivity function $R(\theta)$ is a function of the rocking curve. The beam intensities of the images I_L and I_H, which are taken on the lower side (θ_L) and the higher side (θ_H) of the rocking curve, respectively, can be expressed by Taylor expansion.

$$I_L = I_R\left(R(\theta_L) + \frac{dR(\theta_L)}{d\theta}\Delta\theta_Z \right)$$

$$I_H = I_R\left(R(\theta_H) + \frac{dR(\theta_H)}{d\theta}\Delta\theta_Z \right)$$

The analyzer reflectivity function *R(θ* is an expression of Taylor expansion. From the above two equations, the beam intensity composed of apparent absorption, I_R, and the refraction image angle, $\Delta\theta_Z$, can be obtained.

$$I_R = \frac{I_L\left(\frac{dR(\theta_H)}{d\theta}\right) - I_H\left(\frac{dR(\theta_L)}{d\theta}\right)}{R(\theta_L)\left(\frac{dR(\theta_H)}{d\theta}\right) - R(\theta_H)\left(\frac{dR(\theta_L)}{d\theta}\right)}$$

$$\Delta\theta_Z = \frac{I_H R(\theta_L) - I_L R(\theta_H)}{I_L\left(\frac{dR(\theta_H)}{d\theta}\right) - I_H\left(\frac{dR(\theta_L)}{d\theta}\right)}$$

In general, the images of each side are obtained at the half width of the rocking curve. It makes $R(\theta_L)$ and $R(\theta_H)$ equal with the peak reflectivity normalized to 1.0. Because the rocking curve around the peak is symmetrical, one obtains:

$$\frac{dR(\theta_H)}{d\theta} = -\frac{dR(\theta_L)}{d\theta}$$

Therefore, I_R and $\Delta\theta_Z$ can be shown as

$$I_R = (I_L + I_H)$$

$$\Delta\theta_Z = \frac{0.5(I_H - I_L)}{\frac{dR}{d\theta}(I_H + I_L)}$$

$\Delta\theta_Z$ represents the distribution of angles of refraction in the Z-direction. The refraction intensity, I_R, is expressed by $I_R(dR/d\theta)\Delta\theta_Z$ and is proportional to (I_L-I_H), assuming that the slope of the rocking curve $dR/d\theta$ assumed equal magnitude at the high and low sides. As illustrated in Figure 2-4 by D. Chapman, 1997, the rocking curve FWHM is 4 microradians. The figure also shows both high and low angle sides images.

2.2.2 Diffraction enhanced imaging components

The main components of DEI system are an image plate detector, a monochromator, Bragg analyzer, and a synchrotron radiation source. The DEI group (Zhong, Chapman, at al. 2000) have already established two DEI imaging test facilities using the synchrotron source at the National Synchrotron Light Source (NSLS) of Brookhaven National Laboratory for lower energy range (less than 30 keV), and the Advanced Photon Source (APS) at Argonne National Laboratory for higher energy range (up to 60 keV). The two DEI facilities successfully performed DEI imaging experiments [9].

Z. Zhong, at el [9] reported that the DEI images were obtained using image-plate readers (Fuji Medical Systems, model BAS 2000 or AC3) at the NSLS. Since the Bragg analyzer inverts the beam, the image plate was scanned in the direction opposite to the object's scan direction to avoid blurring the image. The image plate scanner was also tilted to an angle $2\theta_B$ from the vertical direction. The pixel size of the image was 100µm×100µm. Images are read at latitude of 4, and a sensitivity of 400 with 1024 grey levels.

The synchrotron source offers high intensity and good natural collimation of radiation, but it has a continuous spectrum through the entire energy range. The synchrotron radiation makes it possible to select a narrow energy range by a crystal monochromator. According to the experiment by Chapman, at el [1] at NSLS, a silicon double-crystal monochromator was used for selecting narrow radiation energy range. The energy range of the system was 16-25 keV. The beam energy used 18 keV with an energy width of about 1.5eV. The monochromator crystals are silicon (3,3,3) lattice planes. The narrower rocking curve of the Silicon (3,3,3) makes a preferable choice. This choice of lattice planes increased the sensitivity to refraction effects by a factor of five as compared to an experiment that used the silicon (1,1,1) lattice planes.

The x-ray flux of the synchrotron affect the DEI image quality and scan time. According to Z. Zhong, at el [9], the X15A beamline at NSLS has a flux of 1.4×10^{12} ph/s/mm^2/keV at 18 keV (at 200mA ring current) of white beam. This white beam travels thorough a Be window and Al filter, protected from ozone by a helium flow. After the white beam travels through the Be window and Al filter, the specific energy range could be selected by the monochromator. The monochromatic beam is dependent on the crystal diffraction plane. Results of the monochromatic beam, using Si (1,1,1), Si (3,3,3), Si (4,4,4) and Si (5,5,5) are shown in Figure 2-5.

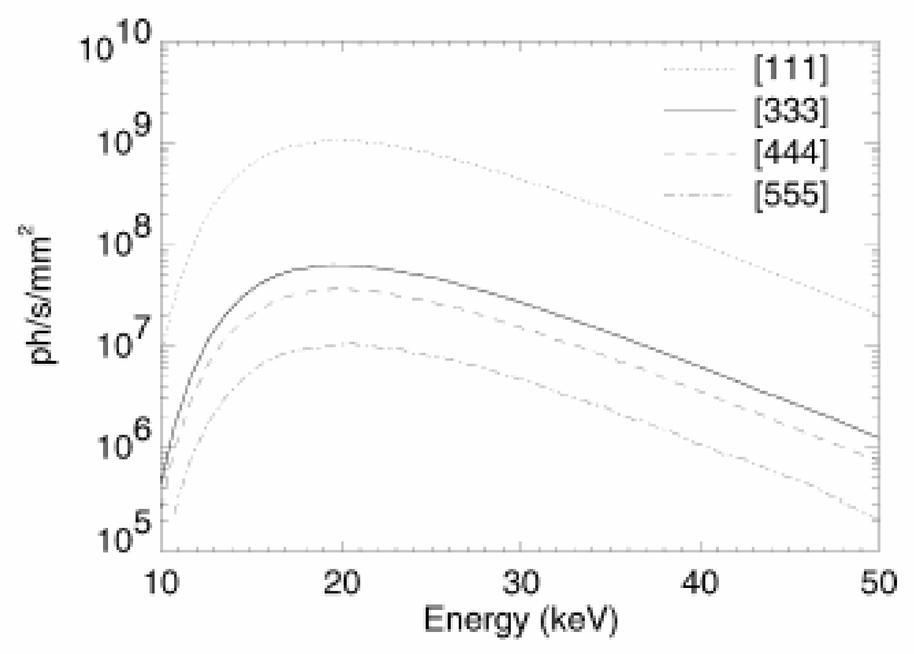

Figure 2- 5 Monochromatic beam flux in the NSLS X15A hutch using silicon [1,1,1],[3,3,3],[4,4,4] ,and [5, 5,5] crystal-diffraction planes (Ref.: Z. Zhong, 2000).

2.2.3 Required X-ray flux

As previously mentioned, the white beam from X15A beamline at NSLS, has 1.4×10^{12} ph/s/mm^2/keV at 18 keV. The scan time, which used this white beam intensity, was 4 to 200 sec. For the purpose of using DEI for mammography, this scan time is appropriate. However, using synchrotron source is not feasible for a clinical DEI system unless DEI facilities to be built at a national laboratory that has a synchrotron source. The size, construction cost, and operation of a synchrotron source are difficulties of applying a synchrotron as an x-ray source for clinical application. A conventional x-ray tube may be used to substitute for the x-ray source, however, conventional x-ray tubes do not specifically provide the characteristics needed for DEI systems. Conventional x-ray tubes have continuous spectrum and low beam intensity as compared to synchrotron sources. The bremsstrahlung radiation from a conventional x-ray tube delivers unnecessary radiation dose to the patient, and does not provide a means by which DEI could be employed. Moreover, the low intensity of the produced x-ray increases the scan time, which is estimated to be approximately between 1,000 to 10,000 second for a conventional source. Such long scanning times are not acceptable to operate a DEI system for clinical use for mammography. It is also important to have a collimated are x-ray beam to provide area magnification for DEI application. A conventional x-ray tube has typically 0.3~0.4 mm focal spot. For a clinically approved DEI mammography unit, the dimension of the beam in the sagittal direction will be 150 mm to get a full field of view. For these reason, a new x-ray source is needed to provide the similar synchrotron characteristics necessary for DEI imaging at clinical practice level.

Several concepts for a new x-ray source were proposed by the NCSU research group (Bourham, Doster, Verghese and Sayers, in collaboration with UNC Chapel Hill Radiology group and others, 2000) [10], such as the shaped-target multi-filament concept, the high-current beam steering concept and the cold cathode field emission concept. The shaped-target multi-filament concept has the most attractive features over other concepts. In this concept, the source design is based on a tilted stationary molybdenum target with the target's surface shaped in a log-spiral. Filaments to be arranged as an array of line filaments, with each filament assembly composed of the individual line filaments and corresponding focus cups. Total emission current of the filament array can be as high as 3A, which will deliver a total power of 180kW to the target for 60kVp operation. The illumination area for this concept is 150 x 150 mm, however, a 50 x 50 mm prototype was proposed. An evolution from this concept is the area x-ray source using concentric circular filaments and a flat (non-shaped) copper target with a layer of molybdenum. The x-ray intensity for DEI can be reached by the above concept, concentric filaments and flat target. This appears as a modification of a conventional x-ray tube utilizing area illumination.

First, increasing the acceleration potential produces higher x-ray intensity. However, generated bremsstrahlung radiation could be reduced and eliminated through Aluminum or Beryllium filter. Second, increasing the electron beam current, which depends on electron emission area from the filament, could increase the x-ray intensity. The typical x-ray tube uses a small line filament, which does not exceed the diameter of the target area. Therefore, the concept of concentric circular, or spiral, filament produces larger electron emission as the emission area increases over the standard small line filament source. The large electron emission area produces higher electron beam current, and higher electron flux, thus increasing the number of electrons illuminating the target over the entire target cross section. Both methods, increasing acceleration potential and using larger electron emission area, result in increased heat loading of the x-ray. The heat loading would exceed the capacity of cooling mechanism of typical x-ray tube, which usually uses a rotating target to spread the heat loading or uses an air-cooling system. Therefore, a concentric filament x-ray source will necessitate an active cooling system for heat removal.

2.3 The area x-ray generator

For this study, the area x-ray generator is basically composed of a stationary target made of oxygen-free copper with a molybdenum layer, a filament assembly composed of three concentric circular filaments, an active cooling system for the target and the overall housing of the source assembly. The core of this research is to investigate the source electrostatics and generation of the electrons and their trajectories, thermal behavior and thermal management, nuclear analysis of x-ray generation and dose delivery, and x-ray shielding and safety.

Electron trajectories and their distribution in the system are determined by the geometry of anode and cathode, and the form of electron acceleration. Thus, an analysis of electron trajectories and their distribution is conducted using electrostatic code (SIMION). As accelerated electrons hit the target, most of their kinetic energy converts to heat thus raising the target's temperature (which may exceed its vaporization temperature), and limits the operational time. The system should operate in a time range not to allow target melting. For this purpose thermal calculations are performed using in-house heat transfer code. The x-ray quality and intensity are related to the target material and the electron accelerating potential, which requires nuclear analysis of x-ray generation; the Monte Carlo code MCNP 4C2 has been used for this analysis.

Chapter 3
Theory

3.1 Electrostatics and electron trajectories

The acceleration and spatial distribution of electron in the x-ray source will affect x-ray generation, target heat loading, and radiation safety concerns arising from electrons bouncing on the interior of the x-ray source housing. Electrons are generated by thermionic emission from a hot filament and are accelerated towards the target by high voltage accelerating potential. Electron trajectories would have different shapes and distributions depending on the form of the accelerating potential, uniformity of the electric field distribution, biasing of the filament cup or using of a backing plate (the later may also be biased). The SIMION 3D 7.0 was used to calculate electron trajectories and distributions on the target surface for various field configurations and biased and un-biased backing plate.

The SIMION 3D code [12] is based on the charged particles optics, electrons or ions. Charged particle optics utilizes the motion of charged particles under the influence of electric, or magnetic fields, or a combination of both. The equation of motion for a charged particle accelerated by a uniform electric field is

$$A = F / M \rightarrow \frac{dv}{dt} = -\frac{eE}{m}$$

where, A is the acceleration, v is the velocity of the particle, and m is the charged particle's mass. The electric field could be substituted for by the negative gradient of the potential, and thus for an electron:

$$m_e \frac{dv_e}{dt} = -eE_X = e\frac{\partial V}{\partial X}$$

from which the electron velocity could be obtained

$$\int_0^{v_e} dv_e = \frac{e}{m_e}\left(\frac{\partial V}{\partial X}\right)\int_0^t dt$$

$$v_e = \frac{e}{m_e}\frac{dV}{dX}t$$

A static uniform magnetic field will not change the velocity of the charged particle but will force the particle to gyrate in a fixed orbit around the magnetic field line. The force equation for a charged particle under the influence of magnetic field is

$$F_m = Q_i(U \times B)$$

where F_m is the magnetic force, Q_i is the charge (for an ion). The force F_m (Lorentz force) is always normal to both B field vector and U velocity component normal to the magnetic field. Trajectories of charged particles are governed by the form of electric and magnetic fields, their spatial uniformity and their time dependence (if any) [12].

The deflection of a charge particle due to electric force may be expressed by electrostatic radius of refraction, which is proportional to the particle's kinetic energy. The orbiting radius due to magnetic force is proportional to the particle’s momentum. The electric deflection is given by

$-eE_n = \frac{mv^2}{r_n}$, and thus

$$r_n = \frac{mv^2}{-eE_n} = \frac{-(m/e)v^2}{E_n} = \frac{-2K.E}{eE_n}$$

The gyration radius due to magnetic field is given by

$$-B_n ev = \frac{mv^2}{r_n}$$

and thus

$$r_n = \frac{mv}{B_n e} = \frac{(m/e)v}{B_n} = \frac{(2mK.E)^{1/2}}{eB_n}$$

, where $K.E. = (mv)^2/2$.

Thus all ions (or electrons) with the same starting location, direction and kinetic energy per unit charge would have identical trajectories in static electric and magnetic fields. The trajectories are not mass dependent in static electric field, but they are mass dependent in static magnetic field.

When the filament emits electrons by thermionic emission, and an accelerating potential is applied, electrons follow the electric field direction towards the target. Although electron current induces magnetic field, however, this self-induced magnetic field is weak and the force equation is governed by the electric force over Lorentz force.

3.2 Target thermal analysis

3.2.1 Heat production

When electrons hit the target, the kinetic energy of the electrons undergoes conversion to x-ray production and heating of the target. Most of the electron's energy is degraded to heat as the result of collisions with outer shell electrons of the target atoms. The heat production at the target could be calculated from the efficiency of the x-ray production

[14]. The efficiency of x-ray production is directly proportional to the atomic number of the target and to the applied potential, as approximately expressed by the following equation.

$$\%efficiency = K \times Z \times kVp$$

where K is constant = 1×10^{-4}, Z is the atomic number of the target, and kVp is the peak voltage. For example, for a molybdenum target ($Z = 42$) and an accelerating potential of 60 kVp:

$$efficiency = 1 \times 10^{-4} \times 42 \times 60 = 0.25\%$$

This means that only 0.25% of the total kinetic energy of the electron beam appears as x-ray and the remaining 99.75% percent as heat in the target.

3.2.2 Heat transfer

The mechanism of heat transfer into the target has the three heat transfer processes, conduction, convection, and radiation; and they occur simultaneously depending on medium. In x-ray targets, the conduction would be dominant among convection and radiation heat transport as the source is under vacuum. However, radiation heat transfer from the hot target follows. In this research, a molybdenum layer is attached to the oxygen-free target, where the later serves as a target structure and cooling material. The heat conduction equation is given by

$$q_x^{''} = -k \frac{dT}{dx}$$

, where k is thermal conductivity of the target material (W/m-K)

For a one-dimensional plane wall, the heat flux $q_x^{``}$ (W/m^2) is the heat transfer rate in the x direction per unit area perpendicular to the direction of transfer, and it is proportional to the temperature gradient, *dT/dx*, in this direction. The proportionality constant *k*, thermal conductivity, is a transport property [15].

The basic three dimensional – time dependent conduction equation is

$$\nabla \cdot \kappa \nabla T + q^{```}(r) = \rho C_p \frac{\partial T}{\partial t}$$

where,

T: temperature (K)

ρ : density (kg/m^3)

κ : thermal conductivity (W/m·K)

C_p: specific heat (J/kg·K)

$q^{```}$: volumetric heat generation rate (J/m^3·s)

3.3 X-ray production

3.3.1 The Bremsstrahlung process

The conversion of electron kinetic energy into electromagnetic radiation produces x-rays. The x-ray source has the filament as the cathode and is negatively charged. The filament emits electrons by thermionic emission. The anode, the target, may be positively charged, or at zero potential with respect to the cathode. The potential difference between the cathode and anode establishes an electric field and accelerates electrons towards the target, thus electrons gain kinetic energy during their travel along the electric field lines. For example, the energies of electrons accelerated by potential difference of 20 and 100 kilovolt peak (kVp) are 20 and 100 keV, respectively [3]. The kinetic energy of electrons converts to both target heating and production of x-rays, where the largest percentage of this energy appears in target heating. When electrons are accelerated and hit the target material, the target Coulomb force would attract and decelerate the electrons, causing a significant loss of kinetic energy and a change in the electron's trajectories. The amount of energy lost in the target during this process generates electromagnetic radiation, bremsstrahlung "breaking radiation", with equivalent amount of the energy.

The distance between the bombarding electrons and nucleus determines the electron energy lost in producing bremsstrahlung, because the Coulomb force between the nucleus and electron is increasing with the inverse square of the distance between them. The electron energy loss could be determined by long or short-range interactions, or by the direct impact on the nucleus. In the long-range interaction the electron energy loss is low and thus the produced photon's energy is also low. The short-range interaction is an interaction at closer distance, where in this process the electron loses more energy than the first case and thus produces higher energy photons. The third process is the direct electron impact on the nucleus, and the electron loses all its kinetic energy and produces much higher energy photons, however, it is an extremely low probability.

3.3.2 The characteristic x-ray

Collisional interaction takes place when the incident electron's energy exceeds the binding energies of the inner shell electron of the target nucleus. The interaction result in ejecting the incident and target electrons, leaving a vacancy at the electron orbit and the atom becomes ionized. The vacancy of the orbit would be filled by the outer orbit electron, which has low energy state. The excess energy is released as a characteristic x-ray photon with energy equal to the difference between binding energies of the electron shells. The binding energy of an orbit electron is unique to each element. Consequently, the emitted x-ray has discrete energies that is characteristic of the element. The K-shell characteristic x-ray energies are shown in Table 3-1 for various target atoms. The discrete energy spikes are superimposed on the continuous bremsstrahlung spectrum. The most prevalent characteristic x-rays in the diagnostic energy range are due to K shell vacancies. The shell capturing the electron designates the characteristic x-ray transition from the L to the K shell, and K_{β} referred to an electron transition form M, N, or O shell to K shell. In case of mammography, Molybdenum is preferred as a target material, which has low energy characteristic x-ray.

Table 3- 1 K-shell characteristic x-ray energies (keV)

Shell transition	Tungsten	Molybdenum	Rhodium
$K_{\alpha 1}$	59.32	17.48	20.22
$K_{\alpha 2}$	57.98	17.37	20.07
$K_{\beta 1}$	67.24	19.61	22.72

3.3.3 Radiation shielding

When ionizing radiations travel through matter, the radiations, especially γ-ray and x-ray, undergo interactions with the material, specifically photoelectric effect, Compton scattering, pair production, and coherent scattering. The interaction of radiation with matter is explained by the probabilistic terms. The probability of the interaction is dependent on the energies of incident radiation. In case of a photon, the pair production is dominant with increased energy. The photoelectric effect has a higher probability for lower energy photons. The specific photon, which has a certain energy range, has coherent proportionality with three interactions. The interaction probability per unit differential path length is fundamental in describing how radiation interacts with matter and is known as the linear attenuation coefficient. It could also be represented by mass attenuation coefficient which is the linear attenuation coefficient divided by the density [16]. The attenuation coefficient of lead, usually used for radiation shielding, is shown in Figure 3-1. When radiation, x-ray or γ-ray, penetrates a material the intensity decreases exponentially. Thus, materials with higher attenuation coefficient are desirable for radiation shielding.

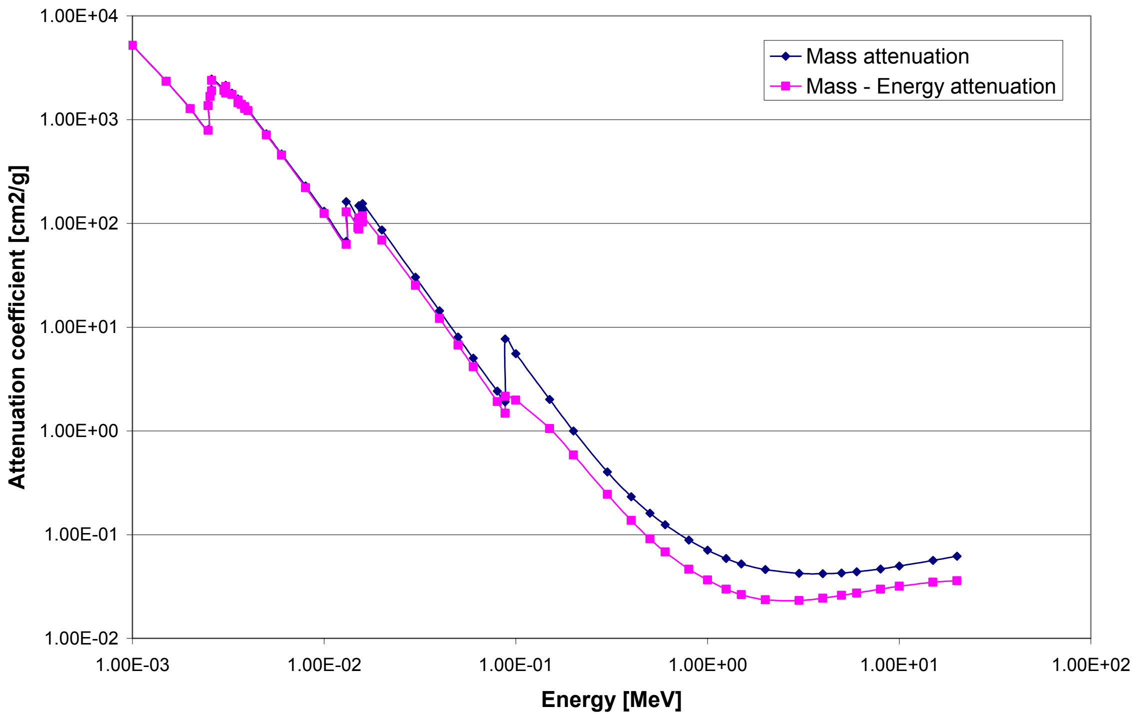

Figure 3- 1 The attenuation coefficient of lead (Ref.: ICRU report 44, 1989)

The photon exposure is defined as the absolute value of the ion charge produced anywhere in the air by the complete stoppage of all negative and positive electrons liberated in an incremental volume of air, per unit mass of air in that volume. The exposure is clearly related to air kerma, but differs in one important respect. The phenomenon measured by the interaction of the photons in the incremental volume of air is not the kinetic energy of the secondary electron, but the ionization caused by the further interaction of these secondary electrons with air. The basic unit of exposure is *roentgen*, abbreviated *R*, which equals to 2.58×10^{-4} coulombs of separated charge per kilogram of air in the incremental volume where the primary photon interaction occur. The conversion factor for kinetic energy to ionization for air is 33.85 eV [17]. The response function of exposure rate is shown in *R* cm^2 [18].

$$R_x = \frac{10^4 kg}{2.58C} R \times \frac{1.602\times10^{-19} C}{ion} \times \frac{10^6 ions}{33.85 MeV} \times \frac{10^3}{kg} \times E\left(\frac{\mu_{en}(E)}{\rho}\right)_{air}$$

$$R_x = 1.835\times10^{-8} E\left(\frac{\mu_{en}(E)}{\rho}\right)_{air}$$

$$\dot{X} = \int_E dER_x(E)\phi(E)$$

The total exposure rate of photon flux could be calculated by integrating over all energy ranges.

Chapter 4

Simulations and Results

In this thesis work, three computer codes were used for the calculations necessary for the proof-of-principle design of the area x-ray generator. The first code is the SIMION 3D [12], which was used to calculate the electron trajectories and their spatial distributions, and to optimize the selection of electric field configuration. Structures of the concentric filaments and target assembly were encoded by a geometry file, which is shown in Appendix I. The electron distribution on the target determines the production of x-ray and heat generation into the target. The Second code is a 2-D cylindrical heat transfer code to calculate the temperature rise of the target, and to help evaluating the operation time under which the target temperature shouldn't exceed the melting point. The third code is the Monte Carlo MCNP 4C2 [19], which was used for calculations of the x-ray production rate with various window options, and was also used for shielding calculation.

4.1 Proof-of-principle apparatus

4.1.1 Filament assembly design

A filament assembly is designed with three concentric circular filaments to provide electron emission from a large area to provide the required area magnification necessary for a DEI system. The filament configuration differs from a conventional x-ray system as the later uses a small line filament inside a filament cup for a spot source. The number density of emitted electrons is determined by the total emitting area. For a line source, such as that of a conventional x-ray tube, longer filament produces higher electron flux, which in turn produces higher x-ray flux. The three concentric circular filaments are designed to produce flux equivalent to synchrotron source. The design parameters of the concentric circular filament are shown in Table 4-1, and an illustration of the filament assembly is shown in Figure 4-1.

Table 4- 1 Concentric circular filament parameters

Material	Tungsten	
Circular filament Radius	Outer filament	0.4749 inch
	Meddle filament	0.3231 inch
	Inner filament	0.1750 inch
Filament diameter	0.05 inch	

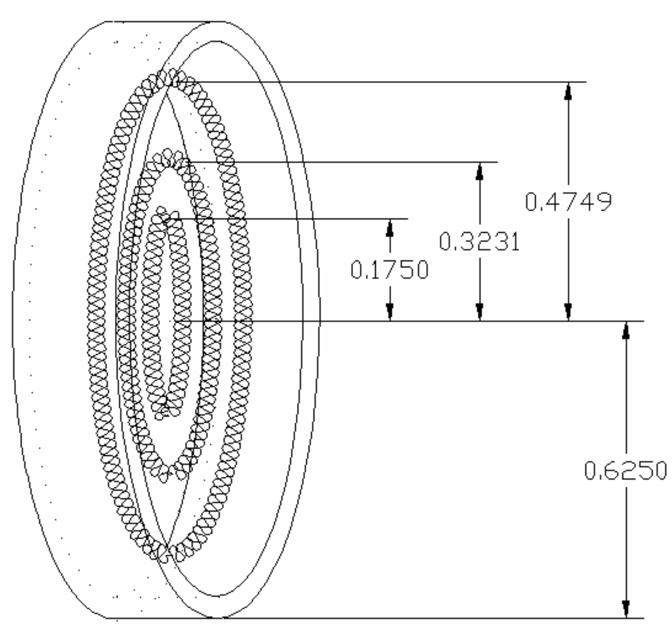

Figure 4- 1 Concentric circular fillament assembly

4.1.2 X-ray target design

There are two aspects for a target design, structure and material. For most conventional x-ray generators, the target may be rotating or stationary. Rotating target provides distribution of the heat over the entire tilted surface of the target and may not necessitate active cooling. The stationary target may be used in systems that operate for very short times; however, active cooling may be necessary. Figure 4-2 shows two conventional x-ray tubes, a rotating target tube (left) and a stationary target tube (right) [3].

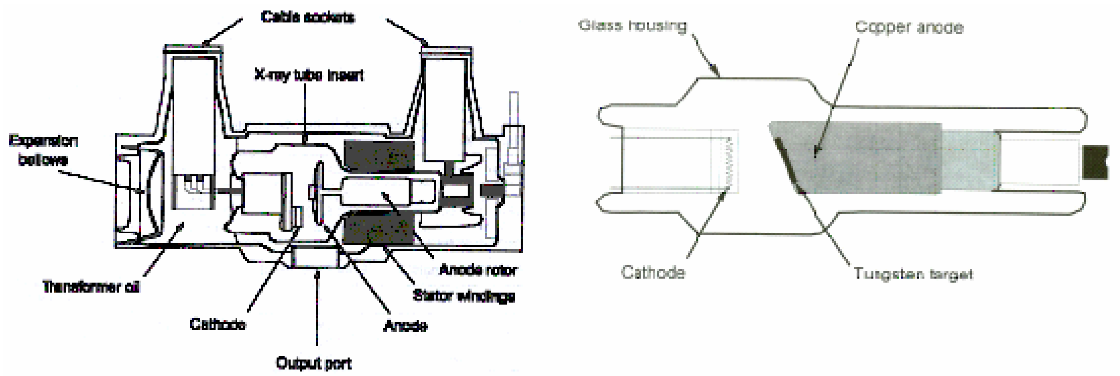

Figure 4- 2 Conventional x-ray tubes; rotating target (left drawing) and stationary target (right drawing). (Ref.: Jerrold T, Essential physics of medical imaging, 2002)

The rotating target has an advantage in terms of better handling of heat loading, as it provides large electron exposed area, and consequently has a decreased average heat loading. The stationary target has more of a simple structure, but its operation time is limited. For the area x-ray source in this study, if to operate at higher beam currents at 60kVp, active cooling will be necessary and may require using a liquid nitrogen cooling circulator to allow for longer operation times sufficient for DEI application. Because of the specific design of the circular filaments to illuminate a larger target area, the target must be stationary in this design. The designed target is made of oxygen-free copper and covered with a molybdenum layer. A liquid nitrogen cold finger will be attached to the back of the target for heat removal. However, the proof-of-principle device may not be equipped with liquid nitrogen cold finger because it is neither intended for longer operation times nor for high beam currents. The proof-of-principle device provides the basic studies in area x-ray production, mapping of electron trajectories and distribution and benchmarking codes' results, however, it is scalable to industrial features with inclusion of forced or liquid nitrogen cooling. The target parameters are shown in Table 4-2, and a drawing of the target is illustrated in Figure 4-3.

Table 4- 2 Target component data

Material	Molybdenum layer on oxygen-free copper	
Length	2.1 inch	
Diameter	1.4 inch	
Melting point [7]	Mo	2623 °C
	Cu	1084.62 °C
Thermal Conductivity [7]	Mo	4.01 W/cm K
	Cu	1.48 W/cm K

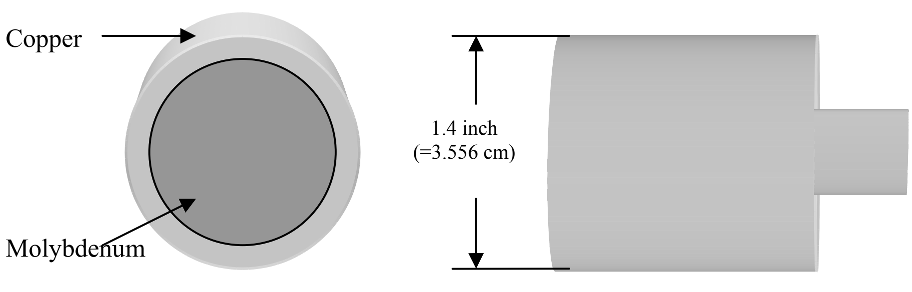

Figure 4- 3 X-ray target for the proof-of-principle device

4.1.3 X-ray source assembly and housing

For the proof-of-principle experimental device, a 6-inch, 6-way cross is used to house the filament-target assembly and to allow for diagnostics to measure the device operational parameters. The experiment is equipped with an air-cooled Alcatel turbo-molecular pump venting to a mechanical rotary pump. A 4-inch extension T-section accommodates vacuum measuring devices, a Convectron gauge and an ionization gauge heads. A pressure of <1x10^{-6} Torr could be reached in about 20 minutes. The filament and target are assembled on one flange with high voltage and filament current feedthroughs. Figure 4-4 shows a drawing of the filament-target configuration and pictures of the filament-target assembly using a line filament source is shown in Figure 4-5. The target is tilted to allow for the take off angle, and thus the x-ray is directed towards the extraction window.

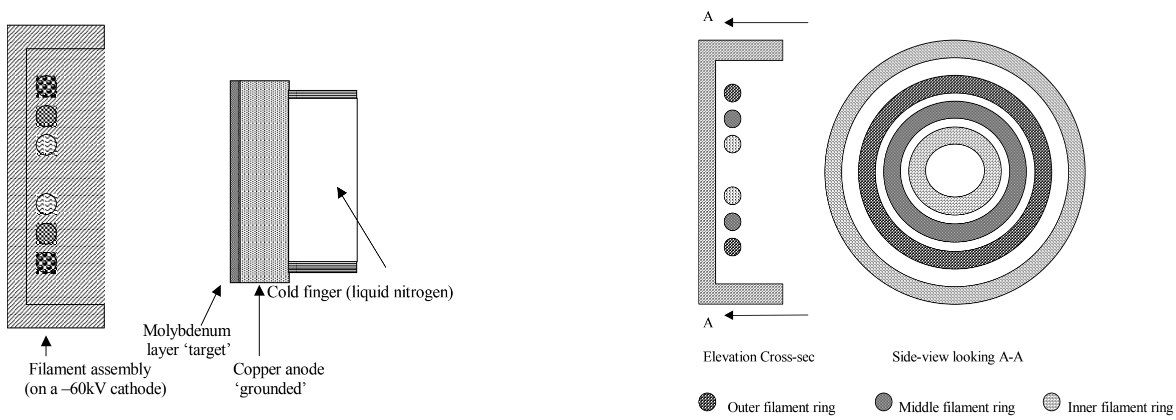

Figure 4- 4 Concept of concentric circular filaments and filament-target configuration

Figure 4- 5 Pictures of the filament-target assembly using a line filament source.

If needed, a liquid nitrogen cold finger feedthrough could be attached through the window across from the back of the target. Other flanges are arranged with instrumentation feedthroughs for experimental measurements. Beryllium or aluminum may serve as the x-ray window material. Optimization of window material and thickness was conducted with the Monte Carlo MCNP code, as will be discussed in section 4.3.3. A schematic of the proof-of-principle experiment is shown in Figures 4-6 and 4-7. Figure 4-7 shows the experimental configuration with instrumentation feedthroughs and the liquid nitrogen cooling option. Additional instrumentation feedthroughs are also installed (not shown in the figure) on the flange opposite to the extraction window. The T-section has an end-on viewing port for infrared thermometry to measure the filament temperature and to monitor the temperature of the filament cup or the target.

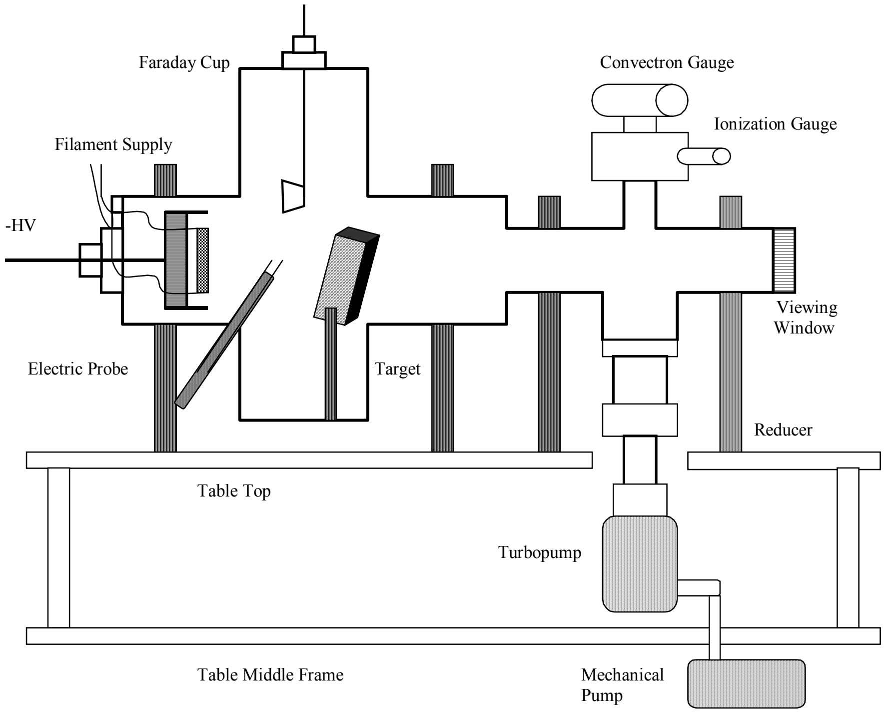

Figure 4- 6 Schematic diagram of the proof-of-principle experimental setup

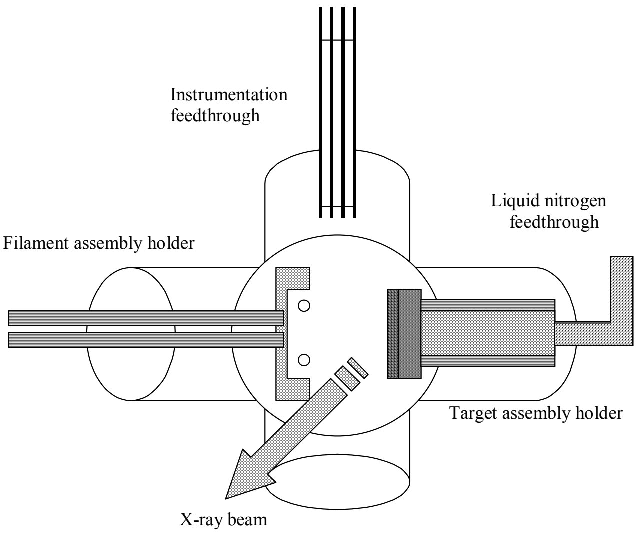

Figure 4- 7 Schematic diagram of the proof-of-principle experimental setup with the liquid nitrogen cooling option. Also shown are the instrumentation feedthroughs

4.2 Electron beam calculations

4.2.1 Thermionic electron emission

Emission of electrons from the hot filament could be calculated from the Richardson-Dushman equation [22], which relates electron current density to the filament's temperature and the filament's material work function. Richardson's equation for thermionic emission is given by:

$$J = A_0 T^2 \exp[-\phi / KT]$$

where,

T : surface temperature of the filament

φ : work function of filament material

K : Boltzman constant

A_0: is a constant $=1.2 \times 10^6$ A/m^{2}K^2 according to the statistical mechanics theory, however, it is not the same for all metals and is 70×10^4 for tungsten (ϕ =4.55V)

It is also possible to calculate the electron beam current from the emissivity of the filament as I = εA, where A is the area of the filament. The emissivity ε of the filament for a specific material is a function of the filament's surface temperature, and could be obtained from available tables, such as CRC Handbook [23]. The emitting area of the filament A = πdL, where d is the filament's diameter and L is the filament's length. For the concentric filament assembly, the total equivalent length of the three filaments is 15.25 cm and the diameter of each filament is 0.127 cm. Table 4-3 shows the surface temperature, corresponding emissivity of tungsten [23], and the calculated beam current for the above filament parameters.

Table 4- 3 Electron beam current as a function of temperature calculated for a tungsten filament. Emissivity of tungsten obtained from CRC Handbook [23]

Temperature [K]	Emissivity [A/cm^2]	Beam current [A]	Temperature [K]	Emissivity [A/cm^2]	Beam current [A]
1500	9.14E-08	5.66E-07	2100	3.93E-03	0.0243
1600	9.27E-07	5.74E-06	2200	1.33E-02	0.0824
1700	7.08E-06	4.39E-05	2300	4.07E-02	0.252
1800	4.47E-05	2.77E-04	2400	1.16E-01	0.719
1900	2.28E-04	1.41E-03	2500	2.98E-01	1.85
2000	1.00E-03	6.20E-03	2600	7.16E-01	4.44

As seen from the table, the filament temperature should be above 2500 K to provide a beam current close to 2 A, in order to produce x-ray flux similar to synchrotron source. The calculation of beam current using Richardson's equation slightly differs from those calculated from emissivity (Table 4-3).

4.2.2 Filament circuit current

The total electric current into the filament could control the desired filament temperature. Assuming all Joule heating of the filament due to circuit current is re-emitted from the filament surface via heat radiation; one may equate the total Joule heating into the filament to the Stefan-Boltzman equation heat radiation equation [24] to correlate circuit current to filament surface temperature, thus:

$$P = I^2 \rho_T \frac{\ell}{A} = A\sigma_T \sigma_s (T^4 - T_0^4)$$

Where,

ρ_T : electric resistivity of the filament

A : filament emission area

σ_T : emissivity of equivalent blackbody

σ_s : Stefan's constant (5.67×10^{-12} w/cm^2k^4)

T : filament temperature

T_0 : temperature of surroundings

The surrounding temperature T_0 may be neglected with respect to the filament temperature (T > 1000°K). For the design parameters of the concentric tungsten filament, the circuit current was calculated for a temperature range between 300 and 2800 °K as shown in Table 4-4. The filament circuit current provides a means by which the beam current is controlled. Combining Tables 4-3 and 4-4 provides a relationship between filament circuit current and electron beam current as shown in Table 4-5.

Table 4- 4 Filament temperature versus circuit current

Temperature [K]	Emissivity [A/cm^2]	Circuit current [A]	Temperature [K]	Emissivity [A/cm^2]	Circuit current [A]
1500	0.192	0.448	2100	0.270	1.037
1600	0.207	0.526	2200	0.279	1.160
1700	0.222	0.617	2300	0.288	1.288
1800	0.236	0.714	2400	0.296	1.420
1900	0.249	0.815	2500	0.303	1.557
2000	0.260	0.924	2600	0.311	1.708

Table 4- 5 Filament circuit current versus beam current

Temperature [K]	Circuit current [A]	Beam Current [A]	Temperature [K]	Circuit current [A]	Beam Current [A]
1500	0.448	5.66E-07	2100	1.037	0.0243
1600	0.526	5.74E-06	2200	1.160	0.0824
1700	0.617	4.39E-05	2300	1.288	0.252
1800	0.714	2.77E-04	2400	1.420	0.719
1900	0.815	1.41E-03	2500	1.557	1.85
2000	0.924	6.20E-03	2600	1.708	4.44

It is worthy to mention that higher beam currents in the range of 2-3 A are required for an industrial scale DEI system, which will necessitate active target cooling. However, for the proof-of-principle experiment, lower beam currents will be used to obtain experimental results on beam uniformity and distribution on the target. Experimental results at low beam currents are scalable to industrial scale device with active target cooling.

4.3 Simulations Results

4.3.1 Electron trajectory simulation

Electron trajectories for the concentric filament-target assembly are simulated using the SIMION code with several options. These options allow for varying electric field configuration by either biasing or floating the base of the filaments' cup (backing plate). The concentric filaments are floating and a separate power supply provides the filament current. The base cup is at negative potential and the x-ray target is grounded. In many x-ray tubes, the filament may be unbiased or biased. Filament biasing could either be positive or negative to shape electron distribution and their trajectories. The filament, in most x-ray tubes, usually has a common connection with the focusing cup such that the cup is at negative potential and the filament is positive with respect to the cup. Figure 4-8 illustrates a standard x-ray filament cup with unbiased and biased connections.

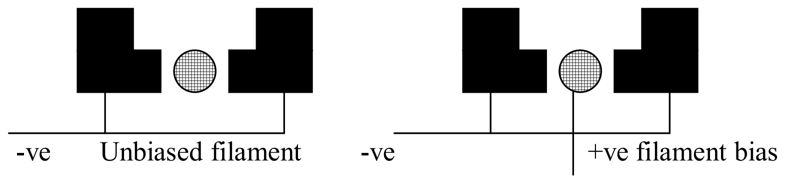

Figure 4- 8 Illustration of standard unbiased and biased x-ray filament cup

For the concentric filament design, the filament supply is floating, however, if desired one of the filament's lead may be connected to the focusing cup such that they together work as a cathode, or the filament may have a high voltage connection different from the cup potential and its supply current floats on top of this high voltage biasing. This design configuration allows for various filament-cup options. Figure 4-9 illustrates the configuration of the concentric filament and focusing cup assembly.

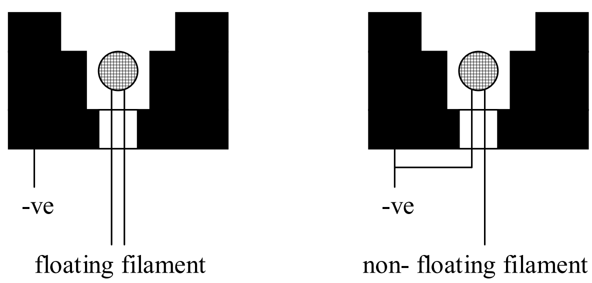

Figure 4- 9 Configuration of the concentric filament and focusing cup assembly

Simulation of electron trajectories, their distribution at the target, and the take off angle has been carried out using the SIMION 3-D 7.0 charged particles' optics code. A geometry code was written (Appendix I) to provide input to SIMION for the filament and target geometry, potential arrays and filament base cup biasing. The simulation generates the electric field profiles, fly the electrons from the filament towards the target, and graphically draw their trajectories and distribution. Optimization of electron flux (beam flux) and uniformity of electron distribution on the target for various options were conducted. The filament cup is named “backing plate” through out this simulation exercises. Optimization would allow for the maximization of electrons landing on the target and minimization of electrons loss due to dispersions. This optimization is necessary to eliminate, or reduce, electron impact on the source housing-chamber, which may result in heat loading of the walls and generating un-wanted radiation.

The backing plate serves as the focusing cup with various biasing options. An example of electron trajectories without and with the backing plate is shown in Figure 4-10 for a 20^{o} target tile angle, where good control on electrons’ dispersion and better focusing onto the target could be achieved. Figure 4-11 shows the electrons’ distribution on the target for the backing plate case. The take off angle determines the focal spot size at the x-ray extraction window. In conventional x-ray tubes, small takeoff angles are used since the electron generation is from an approximate spot filament. In the concentric filament concept, the actual focal spot size is an area on the anode (target), as target illumination in this concept is the entire target surface area. The effective focal length is given by [3]:

$$\textit{Effective focal length} = \textit{Actual focal length} \times \sin\theta$$

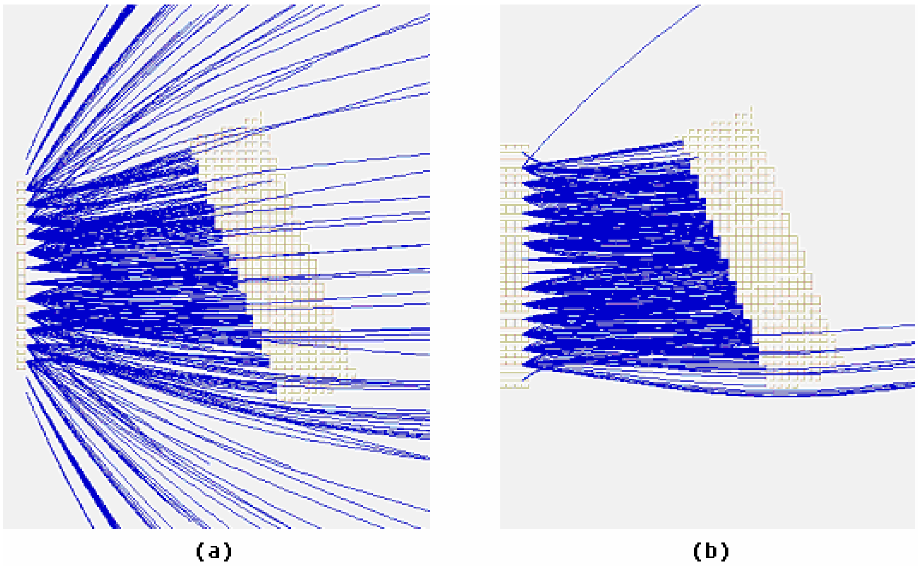

Figure 4- 10 Electron trajectories without (a) and with (b) backing plate, the target is at 20o tile angle with respect to the filament assembly

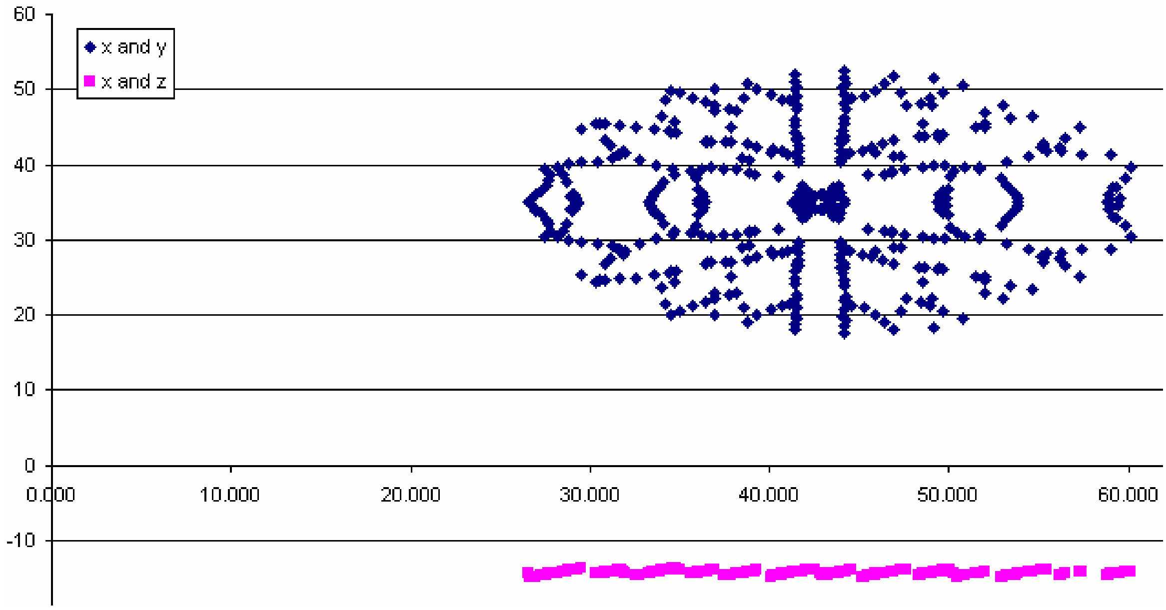

Figure 4- 11 Electrons' distribution on the target, x-y and x-z planes (floating backing plate)

The geometrical configuration of the proof-of-principle experiment allows for a maximum of 22.5° tilt angle. Figure 4-12 is an illustration of the filament and target positions in the proof-of-principle experiment. The effective focal spot is determined by the takeoff angle, distribution of electrons on the target and the spatial and intensity of the electric field.

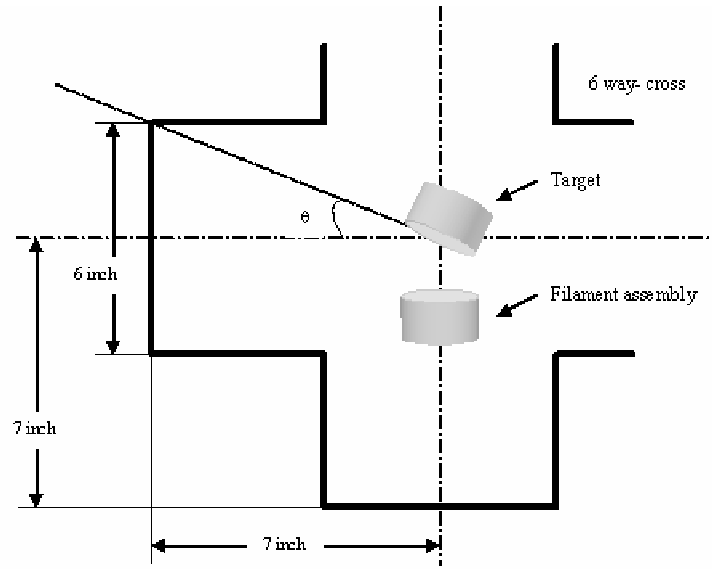

Figure 4- 12 Schematic of filament and target positions in the proof-of-principle experiment, a maximum takeoff angle of θ= 22.5° could be allowed in this geometry

4.3.1.1 SIMION simulation options

Simulation options were performed in three different configurations with each option simulated with five takeoff angles, 0, 5, 10, 15, 20 and 22.5 degrees. The first simulation option has floating backing plate and the filament is acting as the cathode at -60 kV. The second option has the filament acting as a cathode and biased at -12V while the backing plate is at –60kV. The third option has the filament and backing plate connected to each other and at -60 kV.

4.3.1.2 Simulation results

SIMION simulation provides spatial distribution of electrons as they land on the target surface. Axis transformation is required as the target could be tilted to change the takeoff angle. The axis transformation makes it possible to obtain 2-D information from 3-D data. The results of each axis transformation is shown as frequency distributions along x and y directions. Table 4-6 shows simulation results for Option I (floating backing plate and filament acts as cathode at - 60 kV, for all takeoff angle options. Figures 4-13 through 4-17 show 3-D plots of the frequency versus x and y. This configuration develops a hot spot at the center of the target for all takeoff angles indicating that a group of electrons are focused on the target at its center, while other electrons are dispersed and fly away towards the interior of the source housing (also seen in Figure 4-11 with a hot spot at the center).

Table 4- 6 Simulation results, floating backing plate, filament at -60kV

	5 degree		10 degree		15 degree		20 degree		22.5 degree	
node	x	y	x	y	x	y	x	y	x	y
1	25	18	20	18	20	15	22	15	26	16
2	21	26	29	26	29	25	27	24	27	23
3	25	25	29	22	20	23	27	24	27	24
4	34	34	38	34	35	33	38	34	36	33
5	44	44	44	43	48	42	42	40	42	39
6	30	38	32	39	30	36	32	37	30	37
7	80	73	98	70	74	67	76	67	84	68
8	72	75	60	76	78	72	76	72	68	71
9	34	38	36	39	26	36	28	37	28	37
10	42	44	42	43	44	42	43	40	44	39
11	32	34	23	34	24	33	19	34	18	33
12	21	25	24	22	21	23	19	24	25	24
13	23	26	19	26	18	25	20	24	12	23
14	14	19	16	19	21	16	19	16	17	17

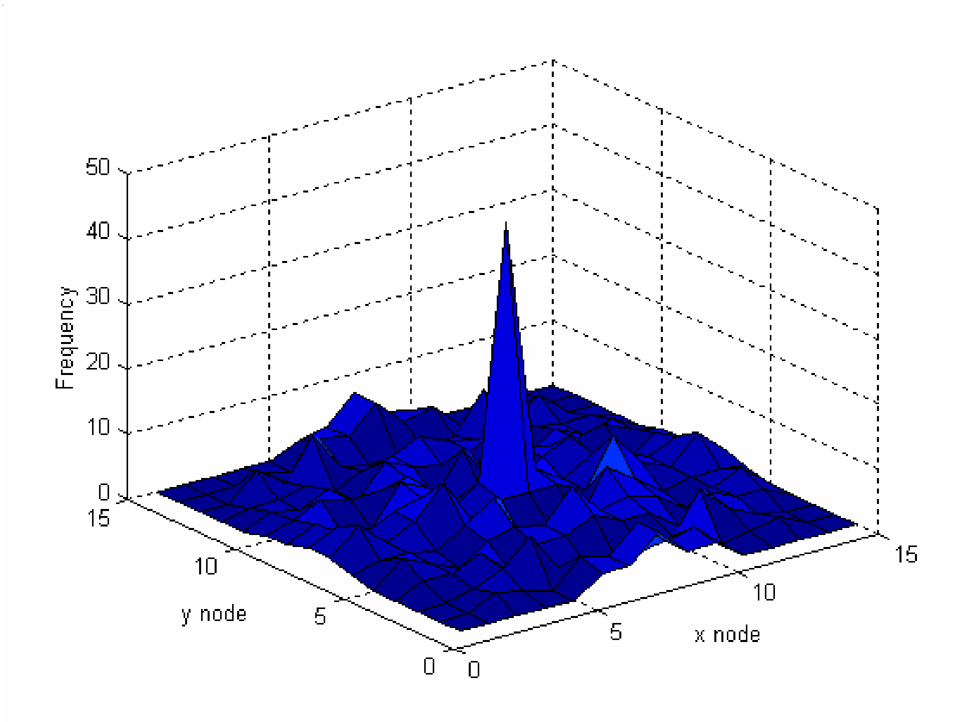

Figure 4- 13 Floating backing plate, filament at -60kV, 5 degree target tilt angle

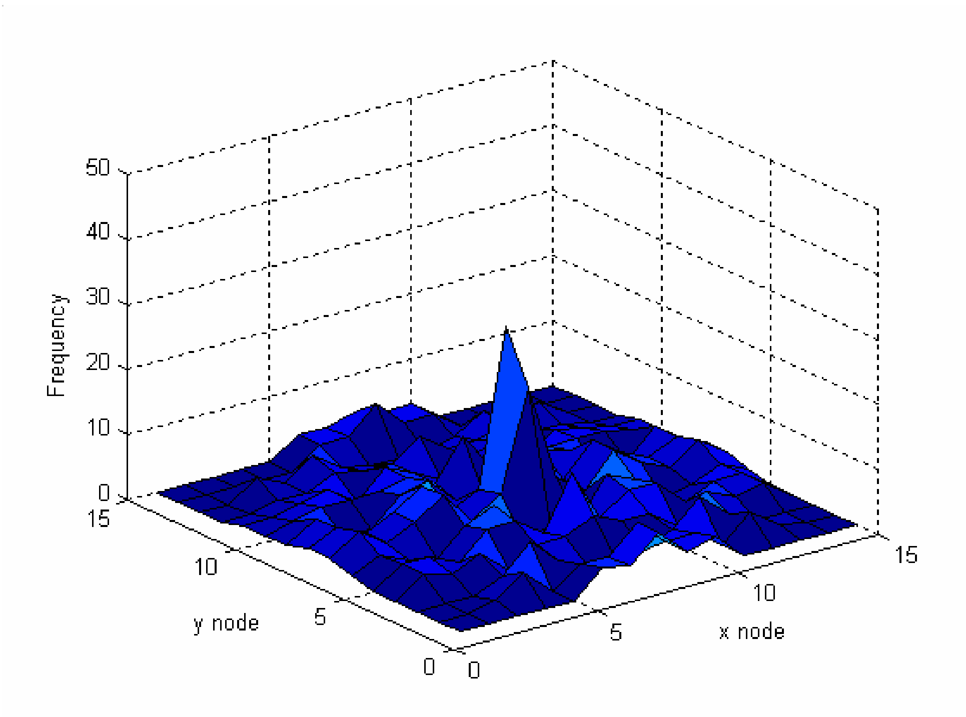

Figure 4- 14 Floating backing plate, filament at -60kV, 10 degree target tilt angle

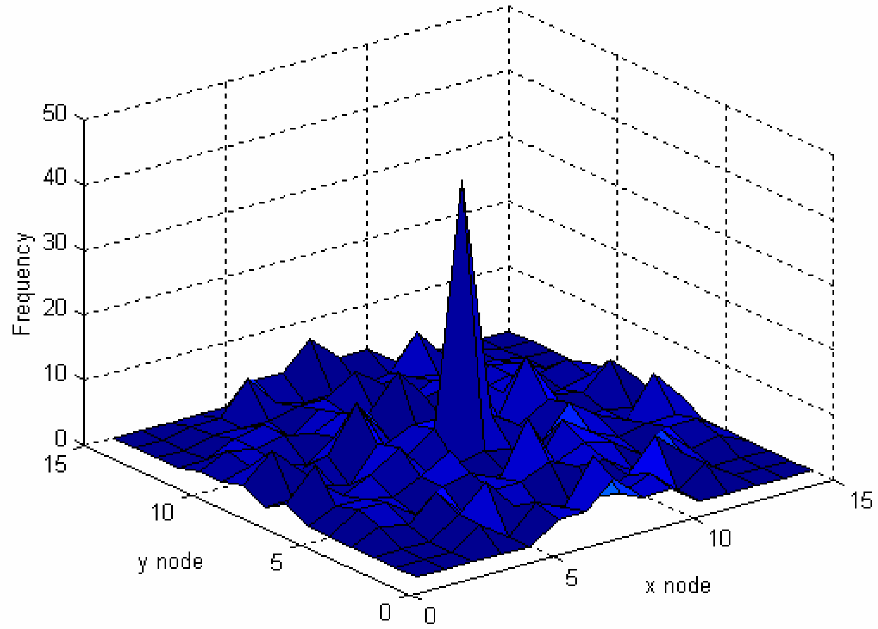

Figure 4- 15 Floating backing plate, filament at -60kV, 15 degree target tilt angle

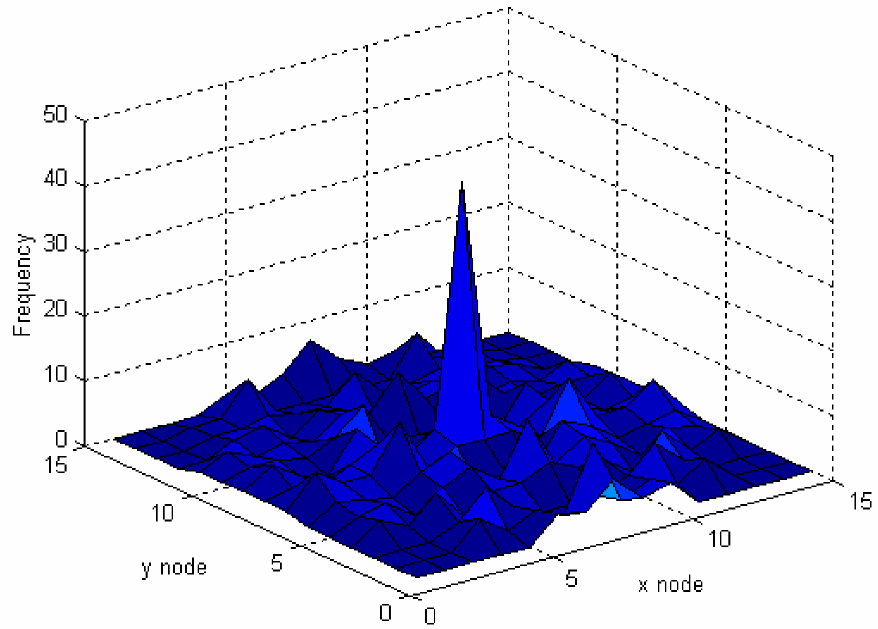

Figure 4- 16 Floating backing plate, filament at -60kV, 20 degree target tilt angle

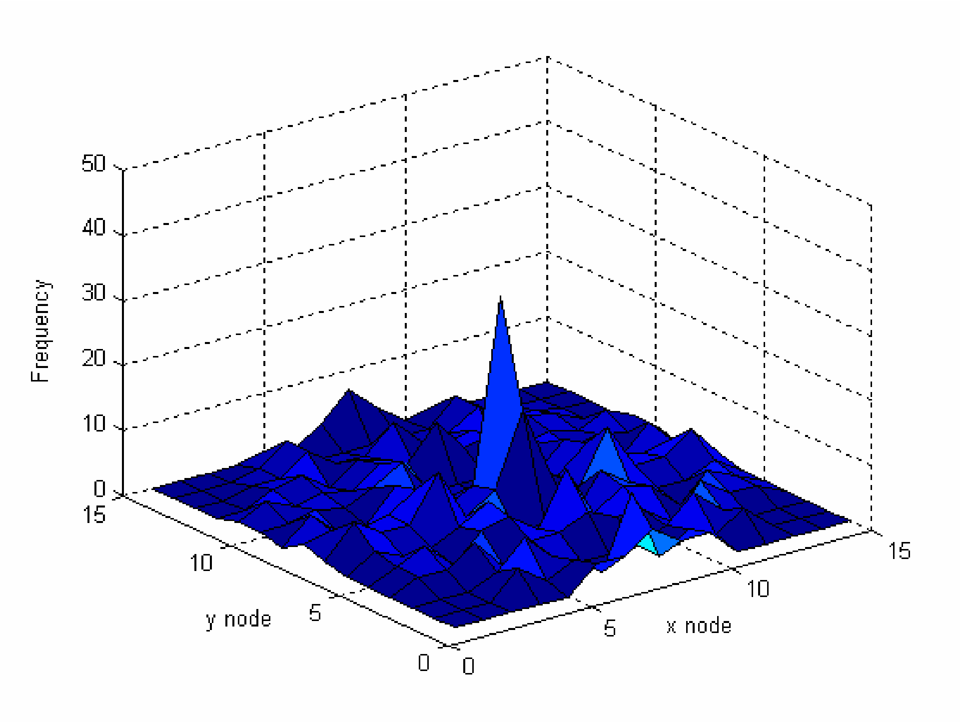

Figure 4- 17 Floating backing plate, filament at -60kV, 22.5 degree target tilt angle

In the second option, where the filament also acts as a cathode and is biased by -12V while the backing plate is at -60kV, the distribution is more uniform and the hotspot moved to lower position of the target surface with increased takeoff angle. However, there is a loss of electron population and many electrons fly away from the target as a result of diverging electric field between the filament assembly and the target. Although target illumination is uniform and reasonable for the production of an area beam, but the expected x-ray intensity will be low. Table 4-7 shows the simulation results, and Figures 4-18 through 4-22 shows 3-D plots of the frequency versus x and y. This option could be used for generating an area x-ray beam by lining the interior of the housing with lead to overcome shielding problems emanating from diverging electrons, and by increasing beam current to increase x-ray intensity, however, the target thermal loading would be very high. Increasing the beam current could be accomplished by increased thermionic emission from the filament, which may lead to either shorter filament lifetime or filament failure at high temperatures; or by increasing the acceleration potential at same beam current, which makes the entire system impractical.

Table 4- 7 Simulation results, Filament at -12V, backing plate at -60 kV

	5 degree		10 degree		15 degree		20 degree		22.5 degree	
node	x	y	x	y	x	y	x	y	x	y
1	8	11	10	11	20	6	16	6	21	13
2	11	10	22	20	24	14	29	14	31	14
3	25	26	38	25	43	24	68	23	52	22
4	47	36	63	33	78	35	84	47	77	36
5	75	55	71	68	84	67	73	69	83	62
6	65	75	103	92	86	80	90	96	88	74
7	97	99	97	105	106	108	89	80	103	88
8	73	118	77	101	81	114	70	96	72	95
9	93	84	77	90	63	90	70	103	77	102
10	83	61	66	52	39	57	41	57	27	74
11	40	42	31	40	28	44	24	43	20	43
12	28	26	16	22	13	23	16	21	14	26
13	14	15	5	16	10	16	5	17	5	13
14	13	13	8	10	12	10	6	9	6	16

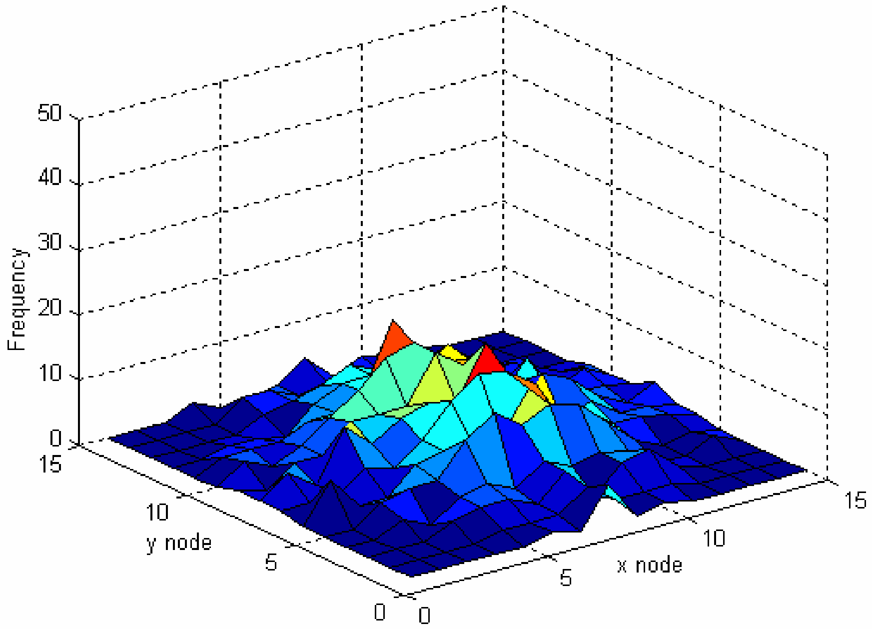

Figure 4- 18 Filament at -12V, backing plate at -60 kV, 5 degree target tilt angle

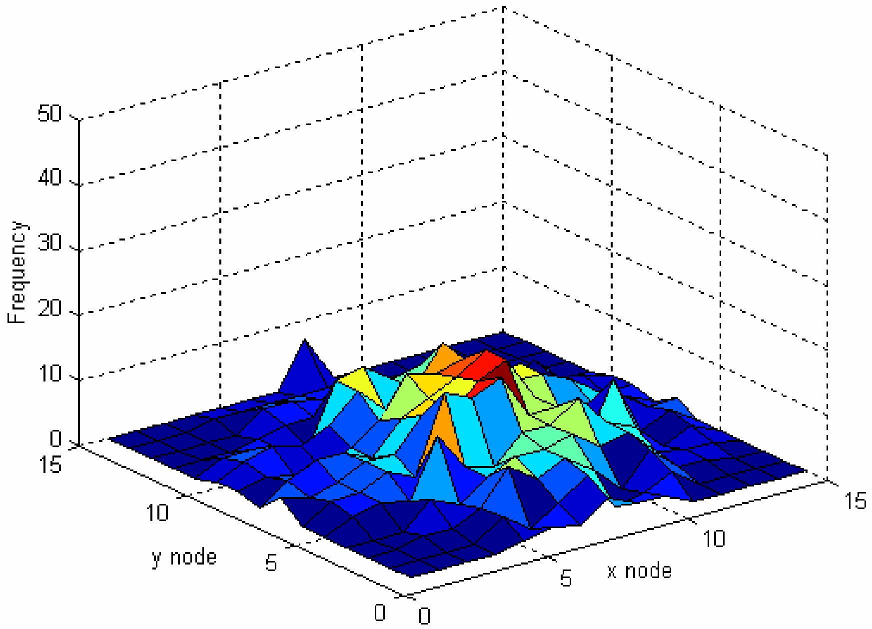

Figure 4- 19 Filament at -12V, backing plate at -60 kV, 10 degree target tilt angle

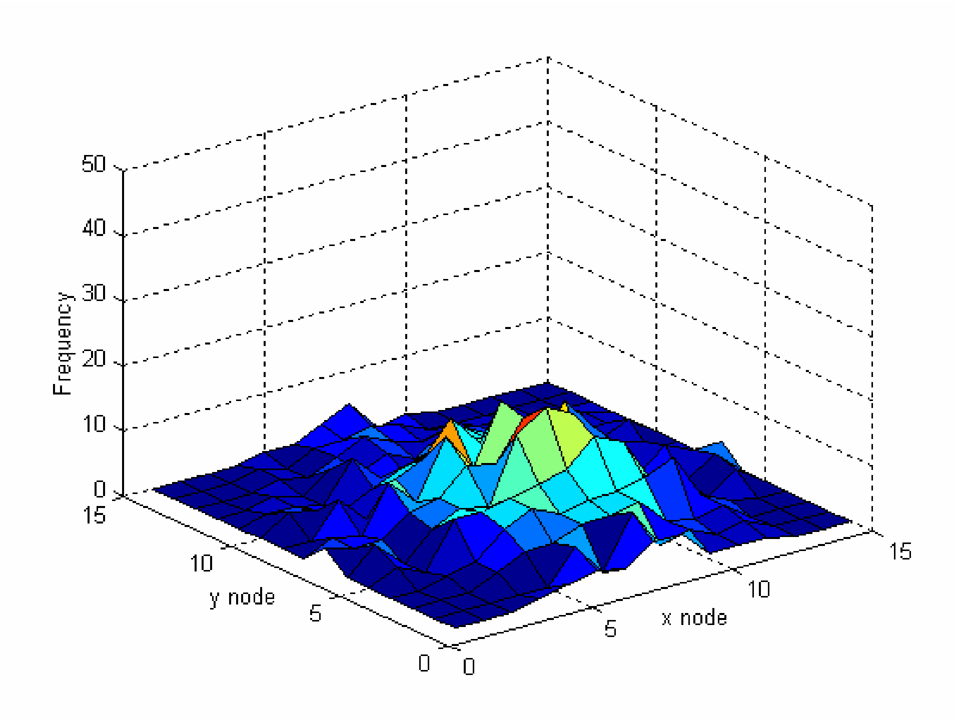

Figure 4- 20 Filament at -12V, backing plate at -60 kV, 15 degree target tilt angle

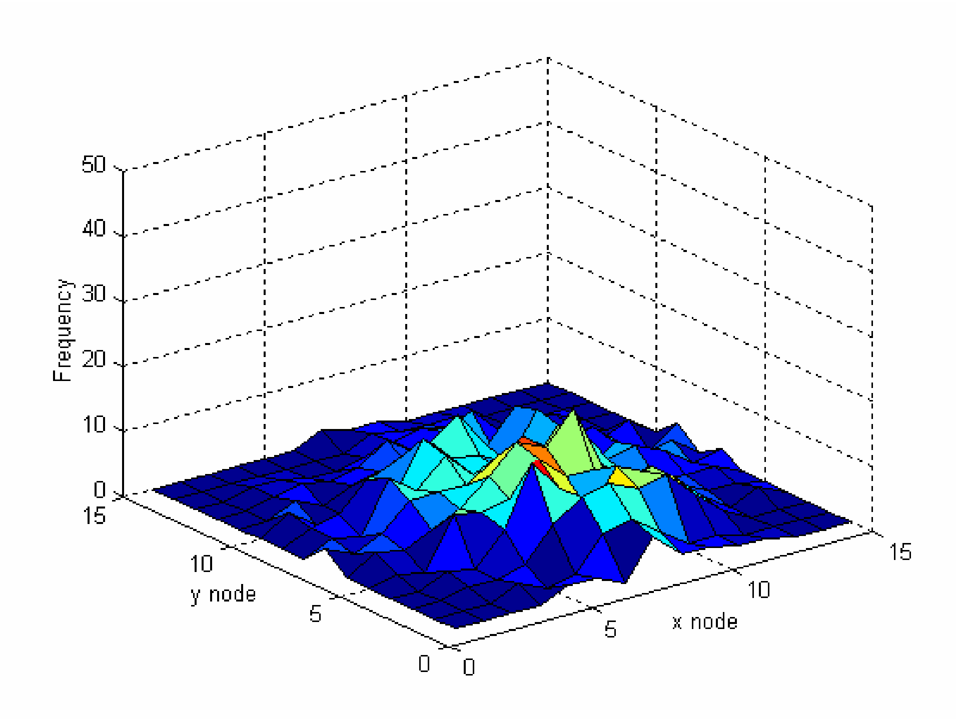

Figure 4- 21 Filament at -12V, backing plate at -60 kV, 20 degree target tilt angle

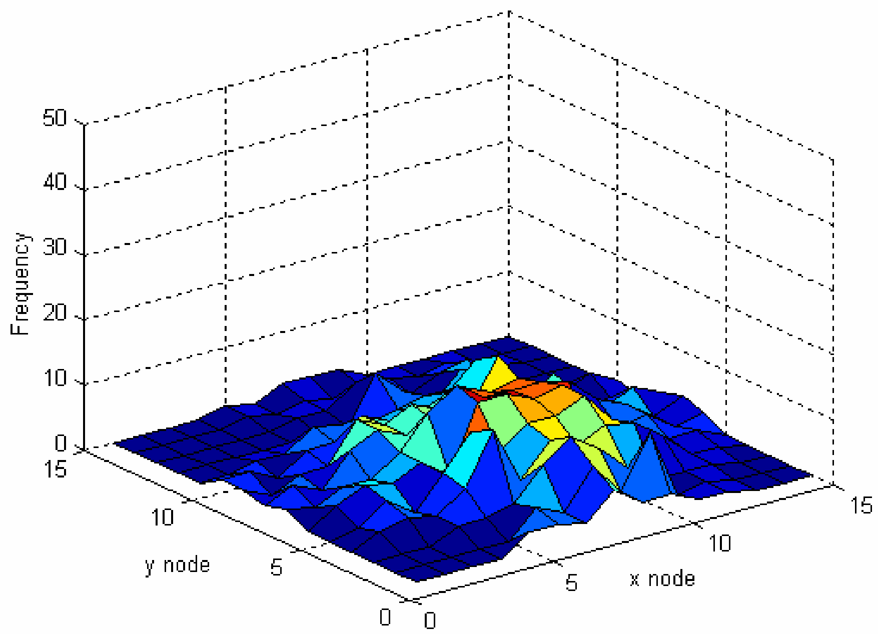

Figure 4- 22 Filament at -12V, backing plate at -60 kV, 22.5 degree target tilt angle

In the third option, where the filament also acts as the cathode at -60kV but also connected to the backing plate, the entire source assembly acts as a traditional x-ray source except that the thermionic emission is a large-area emission versus the spot emission of conventional sources. In this configuration, there is a peak at the center of the target for all takeoff angles. However, the electron trajectories are focused towards the target and few electrons are diverged away, which results in less background radiation. The intensity of generated x-rays will be high and sufficient for DEI application. The hotspot, if to select this option, could be filtered out via x-ray optics or by further optimization in this configuration setup. Table 4-8 shows the simulation results, and Figures 4-23 through 4-27 shows 3-D plots of the frequency versus x and y.

Table 4- 8 Simulation results, Filament at -60kV, backing plate at -60 kV

	5 degree		10 degree		15 degree		20 degree		22.5 degree	
nod	x	y	x	y	x	y	x	y	x	y
1	18	17	18	16	18	17	18	16	18	16
2	43	36	47	37	57	32	49	34	49	34
3	79	68	83	68	79	65	89	64	89	64
4	68	69	62	66	56	68	54	67	54	67
5	74	83	83	81	87	80	81	81	81	81
6	61	74	56	76	56	77	58	78	58	78
7	135	103	138	102	154	99	131	97	131	97
8	107	113	104	112	94	108	107	106	107	106
9	76	75	76	76	74	77	72	78	72	78
10	58	84	59	83	59	82	60	83	58	83
11	75	69	70	66	66	67	50	65	52	65
12	63	66	67	66	51	64	66	64	66	64
13	35	36	25	37	31	32	35	34	35	34
14	18	17	15	16	3	18	13	16	14	16

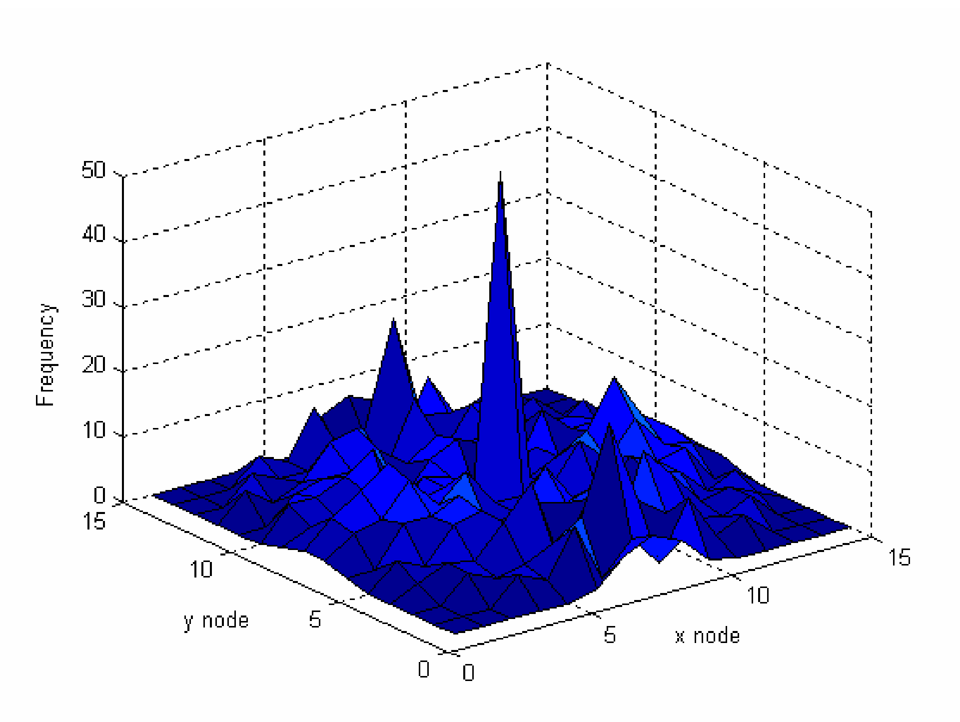

Figure 4- 23 Filament at -60kV, backing plate at -60 kV, 5 degree target tilt angle

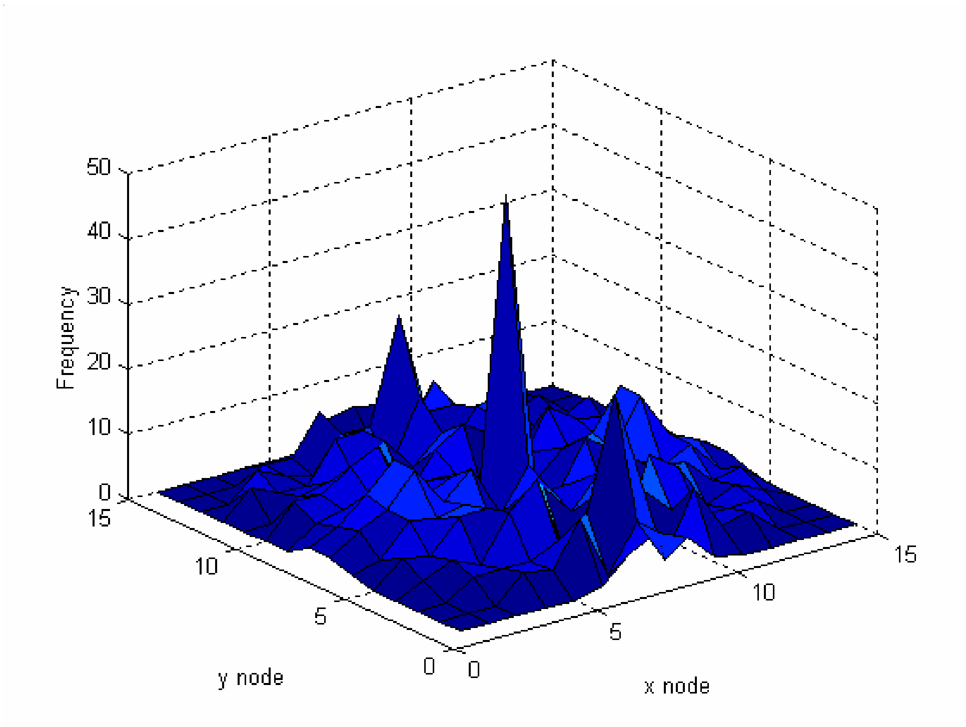

Figure 4- 24 Filament at -60kV, backing plate at -60 kV, 10 degree target tilt angle

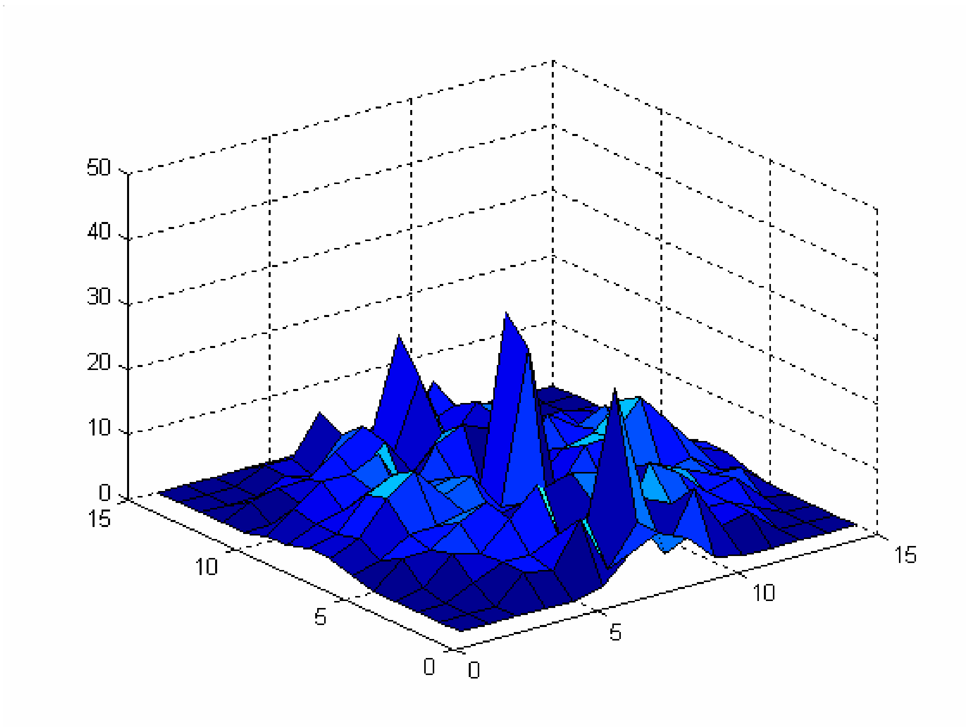

Figure 4- 25 Filament at -60kV, backing plate at -60 kV, 15 degree target tilt angle

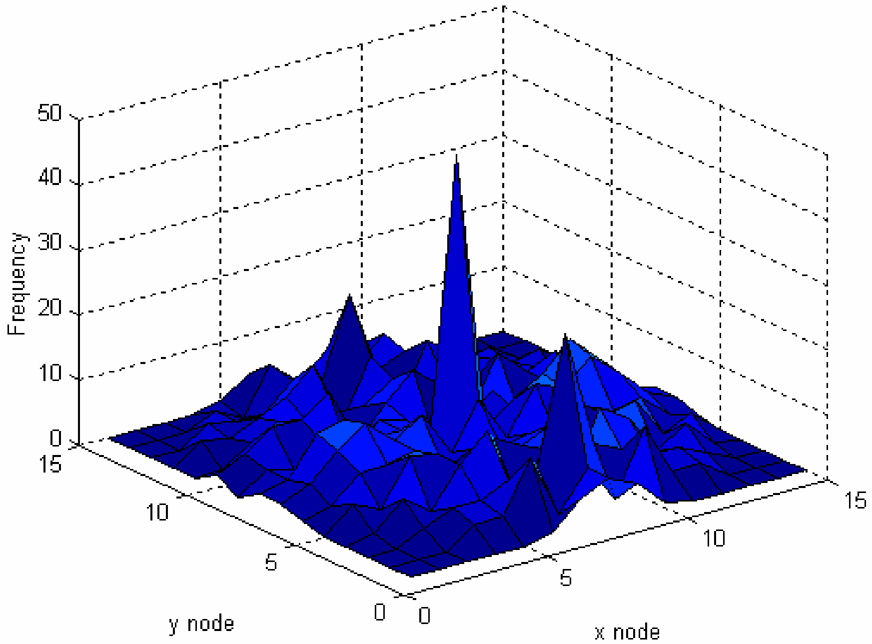

Figure 4- 26 Filament at -60kV, backing plate at -60 kV, 20 degree target tilt angle

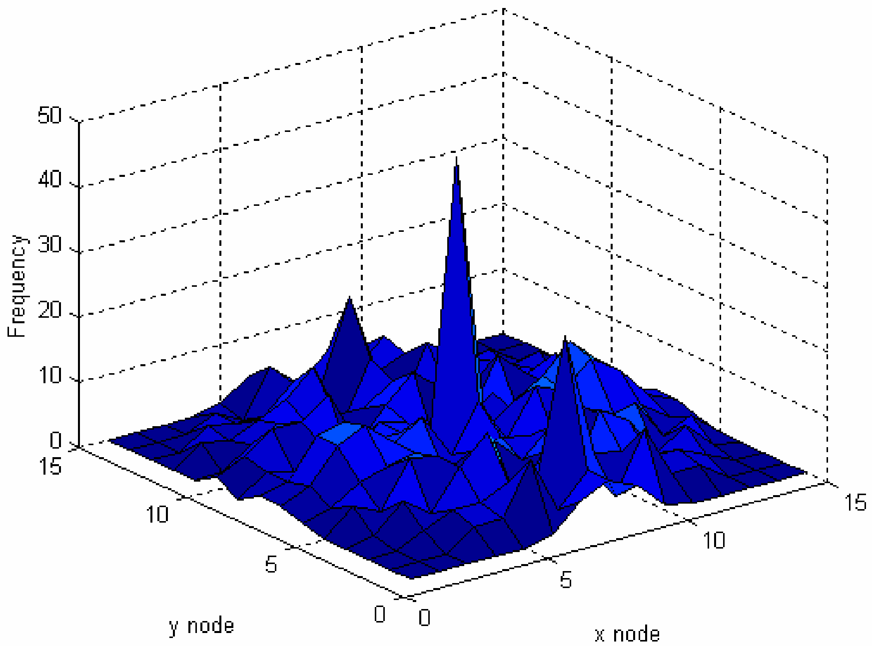

Figure 4- 27 Filament at -60kV, backing plate at -60 kV, 22.5 degree target tilt angle

4.3.2 Target thermal analysis

The impact of the electron beam on the target produces target heating and may raise the target's temperature beyond the melting point. In the target, the main heat transfer is conduction, although the target would re-emit heat via radiation at a slow rate as the entire source is under vacuum. Convective heat transfer could also be ignored in the analysis since the system is under vacuum, 10^{-6} Torr, and there is no flow regime to allow for efficient convection. The target material properties and its geometrical shape are important factors in heat conduction analysis. The target is a thin layer of molybdenum on top of oxygen-free cylindrical copper block. Molybdenum melting point is 2623^{o}C while it is much lower for copper (1085^{o}C), and thus the copper block will reach melting if heat loading is intensive. The thermal resistance of the thin molybdenum layer could also be ignored with respect to the copper block.

Electron heat flux

The accelerated electrons lose their kinetic energy upon their impact on the target, which will be transferred to target heating, as almost 99% of the kinetic energy will be converted to heat. For molybdenum, only 0.25 % of the incoming electrons contribute to the production of x-rays. The heat flux could be expressed in terms of the beam current density:

$$H = I_{BC}\,(Ampere)\left(\frac{Coulomb/\sec}{Amperes}\right)\left(\frac{6.25\times10^{18}\,electrons}{Coulomb}\right)E\left(\frac{eV}{electron}\right)\left(\frac{1.602\times10^{-19}\,J}{eV}\right)$$

$$H = I_{BC}E(J/s)$$

where, E (eV/electron) is the energy of the accelerated electron.

Thermal resistance of target material

The thermal resistance of the target could be approximated to simple slab geometry and assumed to be that of the copper block due to the fact that the molybdenum layer is very thin (molybdenum, about few micrometers, is a layer prepared by sintering on the surface of the copper block). The thermal resistance in the simple slab geometry is given by

$$R = \frac{b}{Ak_c}$$

where, b is thickness, A is the area of slab geometry, and k_c is the thermal conductivity of the slab material. The thermal conductivity of molybdenum is about a factor of 4 higher than that of copper, and thus the thermal resistance of molybdenum is very small compared to the copper block and is neglected in this analysis.

In order to perform thermal analysis, electron beam energy and beam profile at the surface of the target must be used as inputs to the thermal analysis code. This code is an in-house code written by Professor J.M. Doster and can run cases for various geometry and beam profiles. The choice of beam profile is based on the results of the preceding section of SIMION code results. The third option, where the filament acts as the cathode at -60kV and is connected to the backing plate such that the backing plate is also at -60 kV, was chosen as the test case for thermal analysis because it shows the least loss of particles and the best beam focusing on the target. The electron distribution has been converted from Cartesian to radial for a total of 7 radial nodes, and is shown as a histogram in Figure 4-28. Three test cases were considered, beam currents of 3mA, 30mA and 300mA. In all three cases, the spatial distribution of the target temperature rise is obtained as a function of time, with the limiting factor set to the time-to-melting of the copper surface facing the incoming electron beam. The relation between the filament circuit current and beam current could determine the electron beam current.

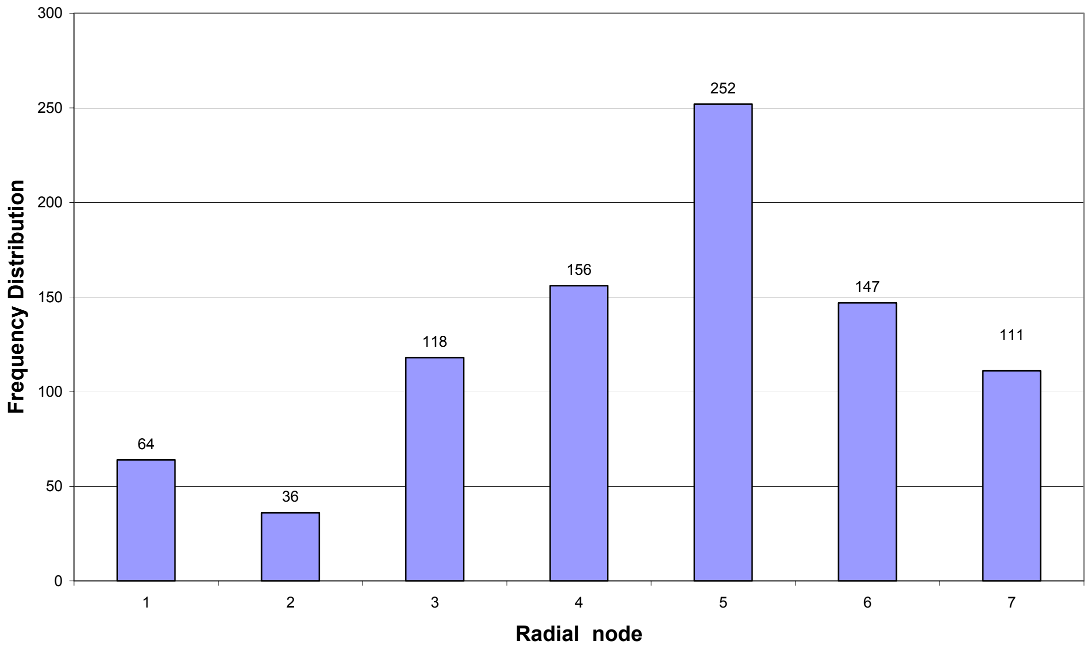

Figure 4- 28 Converted electron distribution as a heat source on the target for the option of the filament and the backing plate connected to each other and at -60kV

The cylindrical target geometry has been specified with radial and axial nodes, each node represents 0.1 inch. The initial target temperature is set to be equal to room temperature. The thermal code input file is shown in Table 4-9.

Table 4- 9 Heat transfer code input data

1) Target Radius (meters)	0.0178
2) Target Height (meters)	0.0711
3) Average Heat Flux (Watts/M**2)	0.1812E+08
4) Target Density (Kg/M**3)	8954.0000
5) Target Specific Heat (J/Kg-K)	383.0000
6) Target Thermal Conductivity (W/m-K)	386.0000
7) Initial Temperature (K)	293.0000
8) Coolant Saturation Temperature (K)	293.0000
9) Ambient Temperature (K)	293.0000
10) Number of Radial Nodes	7
11) Number of Axial Nodes	28
12) Number of Time Steps	1000
13) Time Step Size (seconds)	0.0100

4.3.2.1 Thermal analysis results

For the case of 3mA beam current at 60 kVp acceleration potential, the radial profile of the target temperature shows higher temperature at the center and decays radially towards the outer boundary of the target cylinder. This is because the electron beam profile has a peak at the center, as previously shown in the SIMION code simulation results. The axial temperature distribution shows lower temperature at the end of the cylinder. The temperature of the target's surface reaches 629^{o}K at the center in 450 seconds, which indicates that the operation with such beam current is almost steady state. Figure 4-29 shows the temperature distribution for this case.

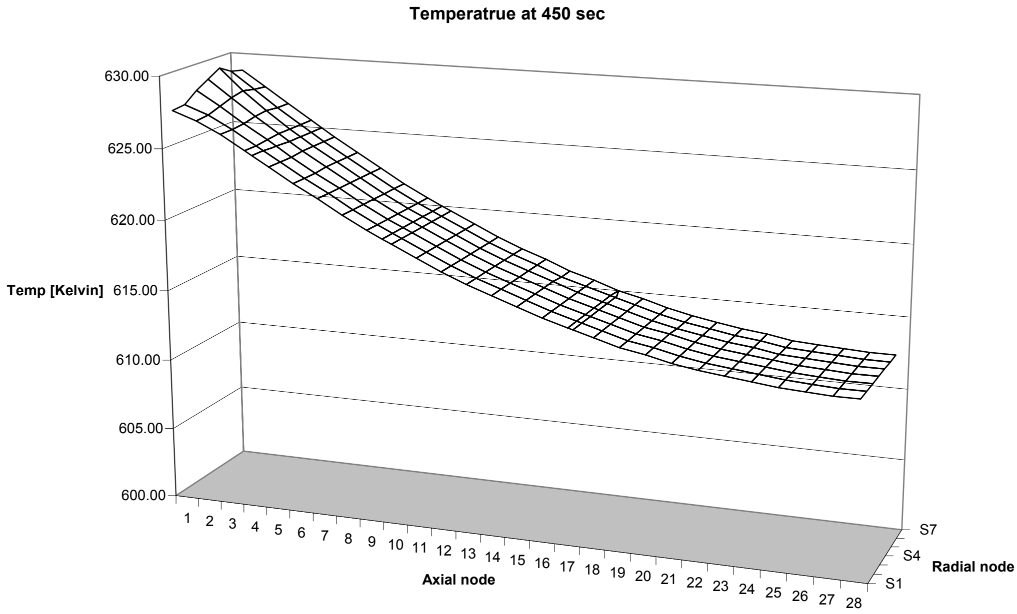

Figure 4- 29 Target temperature distribution for 3mA beam current at 60kV

Increasing the beam current by an order of magnitude, to 30mA, shows similar temperature profiles except that the peak temperature at the center of the target reaches 1355^{o}K in 130 seconds, indicating safe operation for a long time. Figure 4-30 shows the temperature distribution for the 30mA case. Further increase in the beam current to 300mA increases the peak temperature to close to 1400^{o}K in only 3.4 seconds, indicating much shorter allowable operation time. It is also clear that the radial temperature profile is sharper than the 3mA and 30mA cases. Figure 4-31 shows the temperature distribution for the 300mA case. Thus, the possible operation time for these test cases is summarized below:

Table 4- 10 The possible operation time

Beam current	Time (sec)
3mA	> 450
30mA	130
300mA	3.4

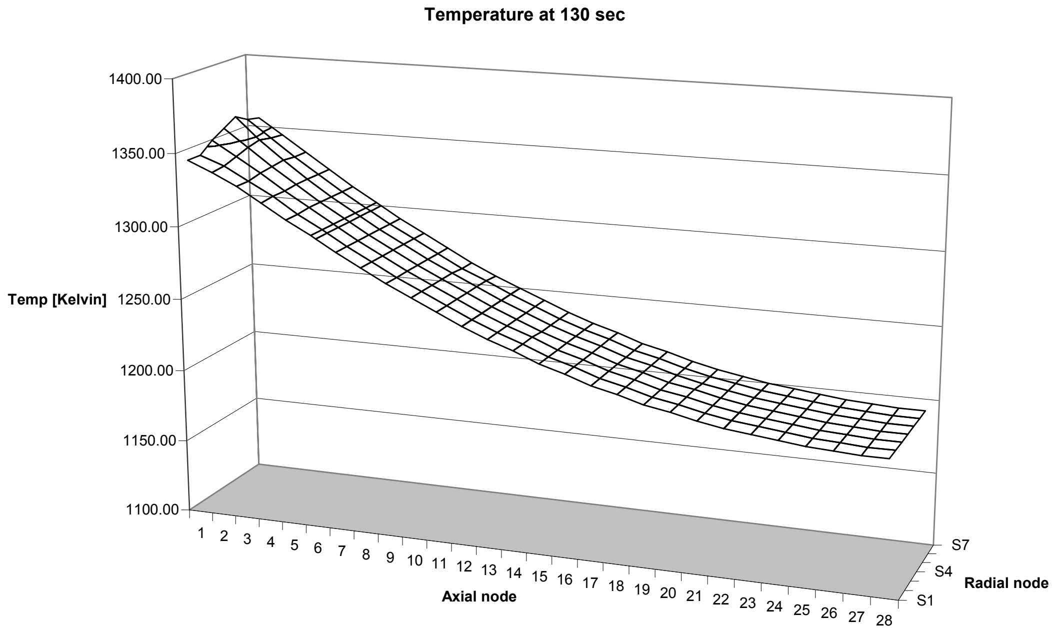

Figure 4- 30 Target temperature distribution for 30mA beam current at 60kV

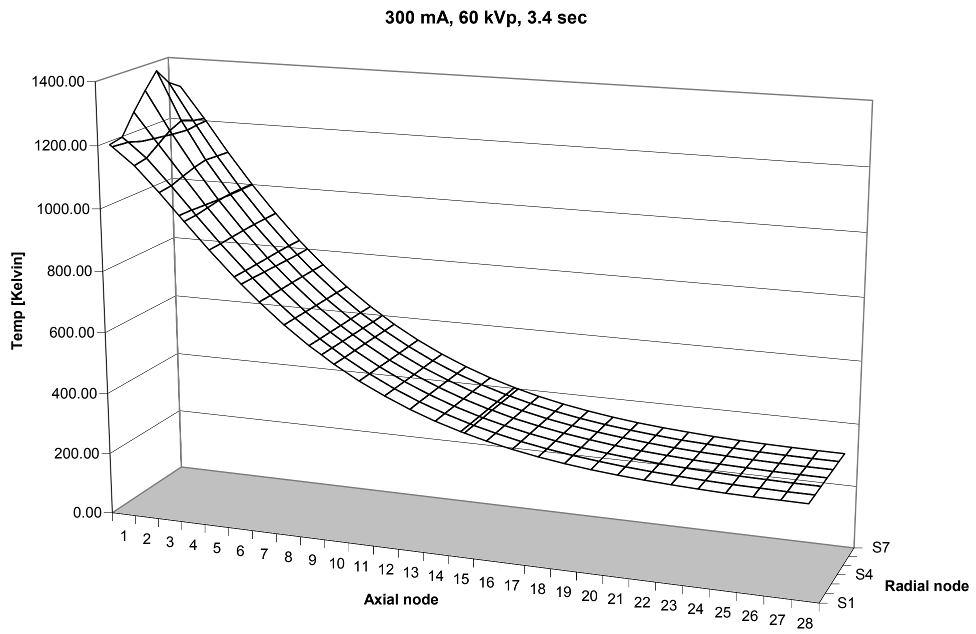

Figure 4- 31 Target temperature distribution for 300mA beam current at 60kV

4.3.3 X-rat production, radiation dose and shielding

The MCNP 4C2 Monte Carlo code has been to calculate x-ray production, radiation dose at the extraction window and radiation shielding of the source chamber. The code calculates production of x-rays from the target and the amount of the x-ray attenuation through the window material. The intensity and quality of x-ray are important factors for DEI imaging quality. The K-shell characteristic x-rays using molybdenum target are the $K_{\alpha1}$ (17.48 keV), $K_{\alpha2}$ (17.37 keV) and $K_{\beta1}$ (19.61 keV). The intensity of produced x-ray at the extraction window will depend on the window material and the thickness of the window. Two window materials, aluminum and beryllium, are used in this simulation with three different window thickness of 0.1mm, 0.05mm and 0.01mm for each material option. Input file for aluminum window and the geometry for MCNP 4C2 code are shown in Appendix II. The selection of these two window materials and their respective thickness for simulation are intended to optimize the maximum flux of the $K_{\alpha1}$ and $K_{\alpha2}$ lines, and possibly the $K_{\beta1}$. Also to help determining the necessary window design to support such thin large area window that can withstand high vacuum without breaking or failure.

4.3.3.1 MCNP simulation results

Simulation results are shown in Table 4-11 for aluminum and Table 4-12 for beryllium, for all thickness options. Shown in the tables are the energies of the $K_{\alpha1}$, $K_{\alpha2}$ and $K_{\beta1}$ versus the probability (particles/cm^2 per total number of source particles) for each window thickness. For a given beam current, multiplying the probability by the total number of the electrons hitting the target (source particles) yields the x-ray intensity for this specific beam current.

Table 4- 11 MCNP simulation results for aluminum window

Al window	0.1 mm		0.05 mm		0.01 mm	
Energy keV	Probability	error	Probability	error	Probability	error
17.38	2.204E-08	0.15	3.476E-08	0.09	6.879E-08	0.09
17.49	3.868E-08	0.12	8.093E-08	0.06	1.239E-07	0.06
19.61	1.445E-08	0.19	2.681E-08	0.10	3.330E-08	0.12
19.97	2.049E-09	0.50	3.332E-09	0.28	5.630E-09	0.30

Table 4- 12 MCNP simulation results for beryllium window

Be window	0.1 mm		0.05 mm		0.01 mm	
Energy keV	Probability	error	Probability	error	Probability	error
17.38	7.764E-08	0.08	7.825E-08	0.06	7.859E-08	0.08
17.49	1.441E-07	0.06	1.563E-07	0.04	1.490E-07	0.06
19.61	3.651E-08	0.12	4.101E-08	0.08	3.803E-08	0.12
19.97	6.073E-09	0.29	5.618E-09	0.21	6.071E-09	0.29

Aluminum window results show increased probability with decreased window thickness, while there is no significant change for beryllium windows. This means that achieving higher x-ray intensity using aluminum window would require a very thin window, which imposes structural difficulty for a large window under high vacuum. For beryllium, it appears that the window thickness is not a factor and a thicker window might be used. This may be helpful in the engineering design of the window with stronger structure integrity. The MCNP results for the entire energy range is shown in Figure 4-32 for the aluminum window, Figure 4-33 for the beryllium window, and a comparison of both is given in Figure 4-34.

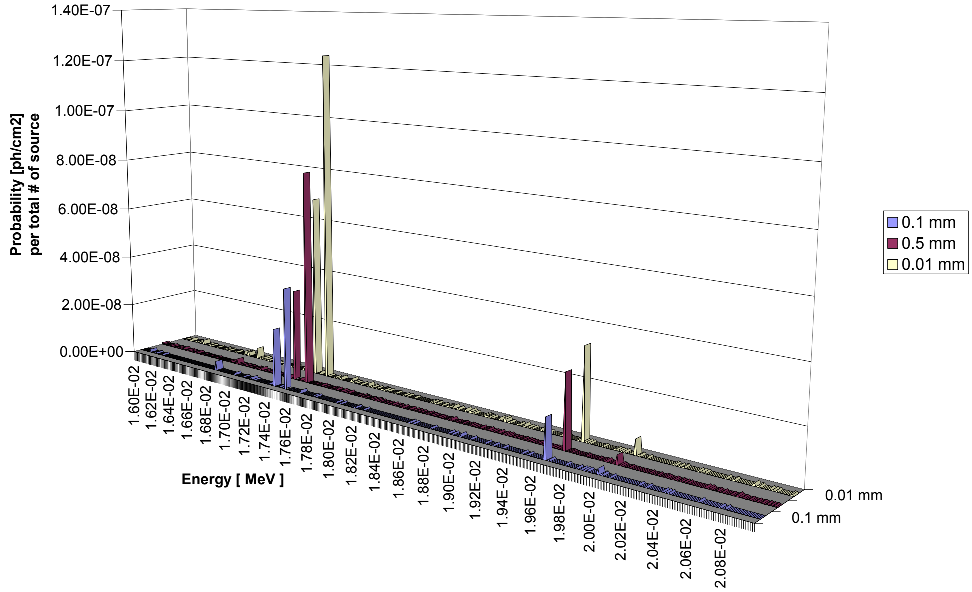

Figure 4- 32 MCNP simulation results for aluminum window options

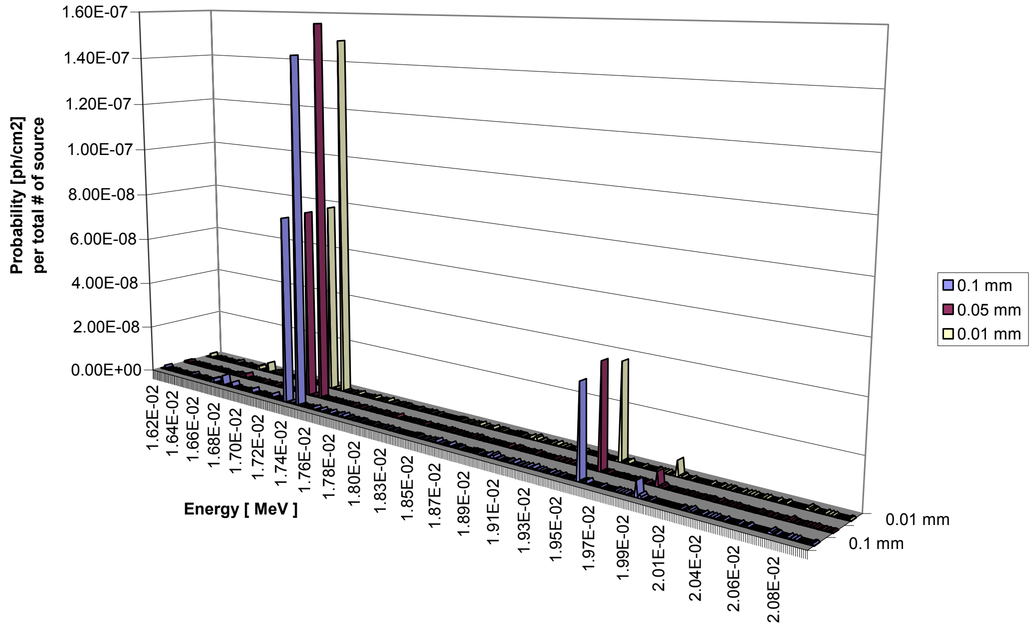

Figure 4- 33 MCNP simulation results for beryllium window options

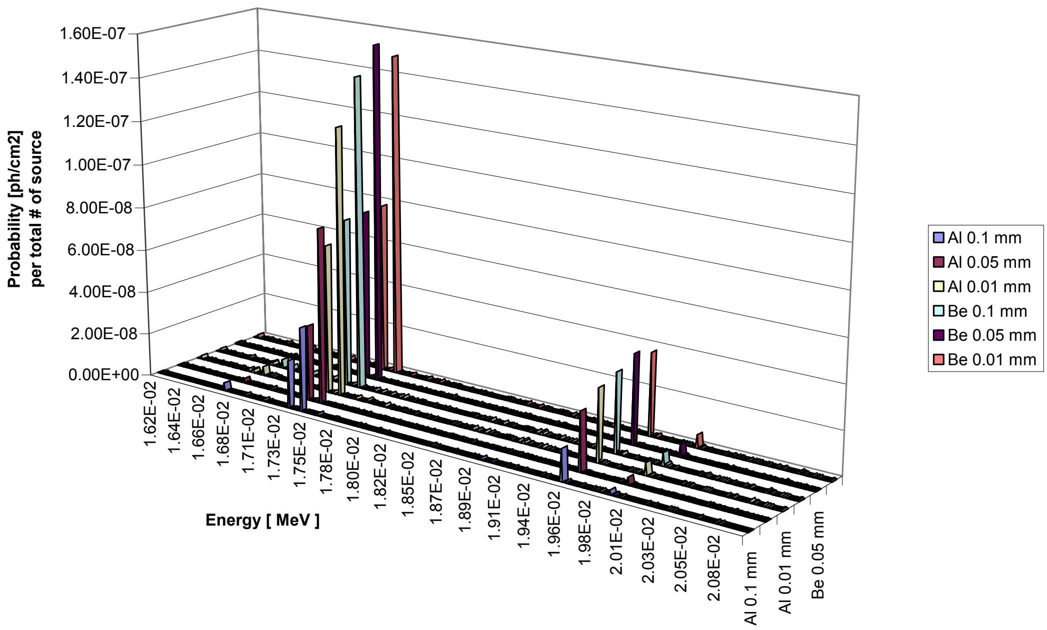

Figure 4- 34 Comparison between aluminum and beryllium window options

4.3.4 X-ray intensity for aluminum and beryllium windows

The x-ray intensities can be calculated from the MCNP results by applying the calculations of Tables 4-11 and 4-12 to each beam current case. The intensity of generated x-ray is obtained from the probability (MCNP results) for the line of interest multiplied by the total number of electrons (particles/cm^2/sec) that corresponds to the beam current. For beam current between 0.001 to 4.0A, the x-ray flux is calculated for each window option. The $K_{\alpha 1}$ x-ray flux for aluminum window options is plotted versus the beam current, as shown in Figure 4-35. To achieve an x-ray flux (~10^{12} ph/cm^2/sec), the beam current must be 4A for 0.1mm aluminum window, 2A for a 0.05 mm thickness and 1.5A for a 0.01mm thickness. For all above cases, the window thickness is an engineering difficulty.

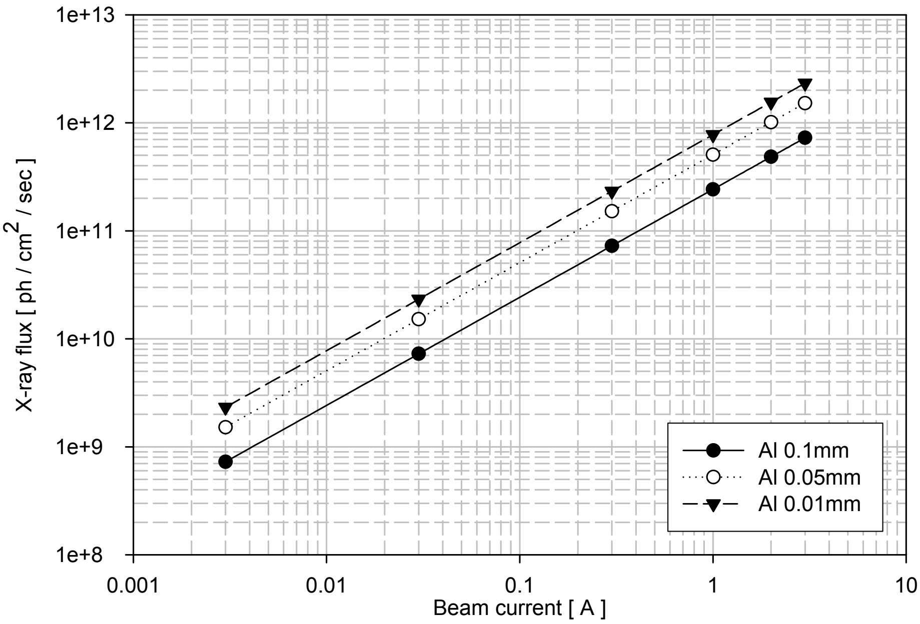

Figure 4- 35 $K_{\alpha 1}$ x-ray flux with Al window options

The $K_{\alpha 1}$ x-ray calculated flux for beryllium window options is plotted versus the beam current, as shown in Figure 4-36. To achieve an x-ray flux ~10^{12} ph/cm^2/sec, the beam current would be 1A for all investigated window thickness options. This beryllium window option has an advantage over aluminum because the window could be thicker to provide structural integrity and facilitate engineering design and manufacturing. Furthermore, the heat loading on the target would be much less as the beam current is a factor of 3 less than that for aluminum.

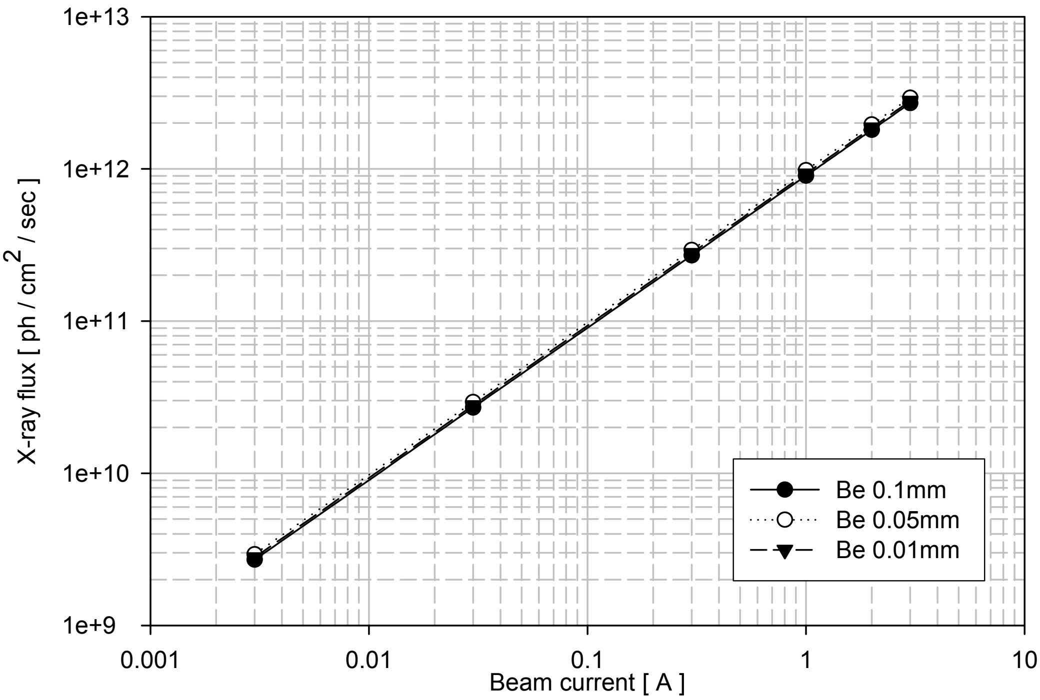

Figure 4- 36 $K_{\alpha 1}$ x-ray flux with Be window options

4.3.5 Shielding consideration

Radiation shielding is important for the safe operation of x-ray devices, even for low-energy x-ray systems. Although the design features provide a less dispersed electron beam on the target, and the choice of the takeoff angle could eliminate stray radiation, however, electrons flying away from the target and impinging on the stainless steel housing structure could generate undesired radiation. The generated x-ray from the target may not completely reach the window and some scattered radiation may take place. To evaluate radiation shielding, a worst-case scenario has been considered by assuming that the generated x-ray hits the stainless steel wall (0.3 cm thickness), attenuated by the wall, then further attenuated by the lead shielding. It was also assumed that attenuation in the air gap between the stainless steel wall and the lining lead is negligible. Exposure rate response function is given by

$$R_x = 1.835 \times 10^{-8} E \left(\frac{\mu_{en}(E)}{\rho} \right)_{air}$$

where the equation represents the exposure rate in air outside the shielding after being attenuated in the stainless steel wall and the lead shielding liner, as explained in Chapter 3, section 3.3.3., and illustrated by the following drawing:

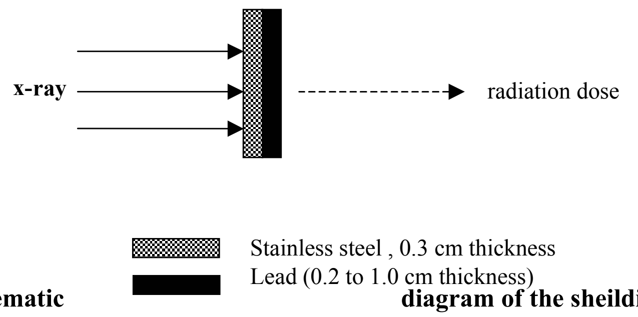

Figure 4- 37 Schematic diagram of the sheilding calculation

Simulation using MCNP code has been performed for 0.3cm iron, as an approximation to stainless steel, and using lead as shielding material surrounding the entire device. Calculations are performed for lead thickness of 0.2, 0.4, 0.6, 0.8 and 1.0 cm. The low energy attenuation coefficient of lead has been obtained from extrapolation of available lead data and is shown in Figure 4-38 [25].

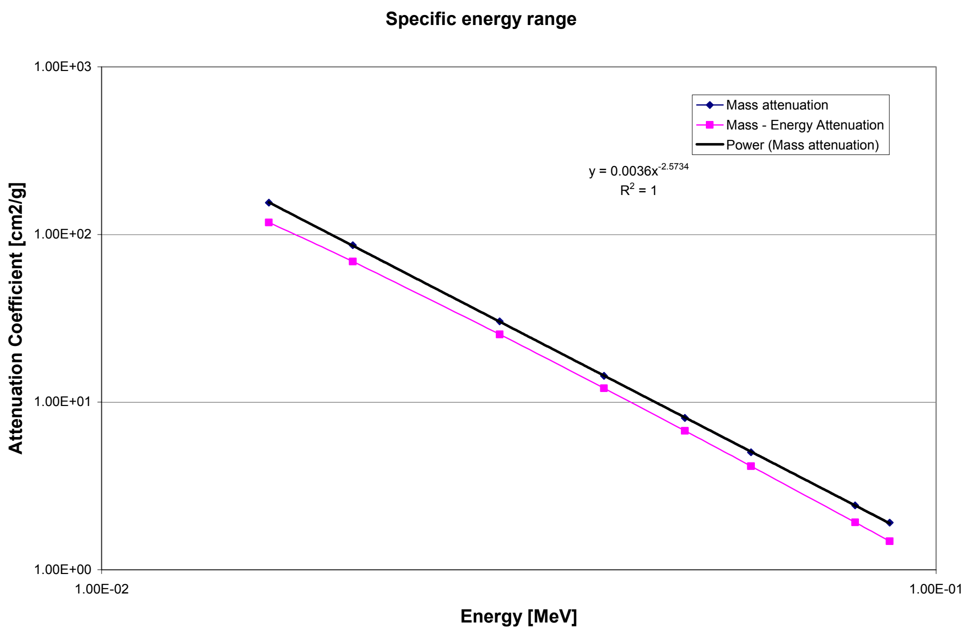

Figure 4- 38 Coefficient of lead in the low energy range (Ref.: ICRU report 44, 1989)

The exposure rate (mR/hr) is obtained over a wide range of beam current. The relation between the beam current and circuit current has been used to plot the exposure rate versus the circuit current, as the later is to be used to control the entire operation of the system. Results of exposure rate versus circuit current are shown in Figure 4-39.

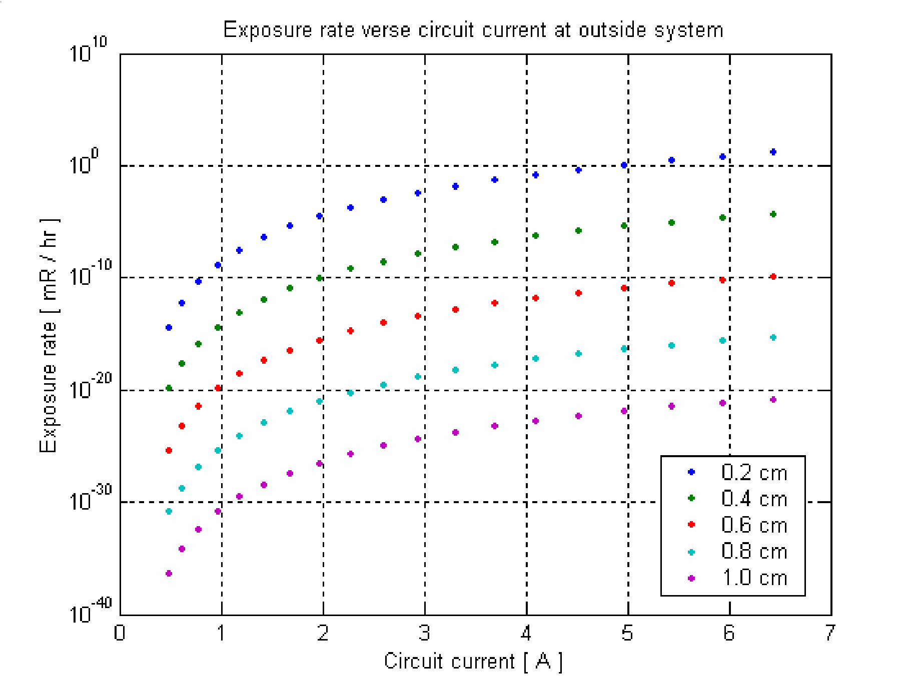

Figure 4- 39 Exposure rate versus circuit current

As has been shown in the calculations of the beryllium window, a 1A beam current would be sufficient to generate x-ray flux ~10^{12} ph/cm^2/sec. Hence, for a 1A beam current, the circuit current should be 4.7A. As seen from Figure 4-38, the radiation exposure if using 0.2cm lead lining would be 1mR/hr. An increased lead thickness to 1.0cm reduces the radiation exposure to ~ 10^{-22} mR/hr. A safe radiation shielding would be sufficient by using 0.4cm lead lining as the corresponding radiation exposure will be less than 10^{-5} mR/hr.

Chapter 5

Conclusions

The research of this thesis focuses on computational studies to develop an area x-ray source that can replace the need for a synchrotron source for diffraction-enhanced imaging for mammography and industrial applications. The features of this area x-ray source are based on generating electrons from three concentric circular filaments to provide an area electron flux, with a 60kV accelerating potential. Study of electron trajectories and their distribution at various tilt angles of the target was completed using the SIMION 3D code. Heat loading and thermal management is studied using an in-house developed thermal and heat transfer code. X-ray flux and energy distribution for aluminum and beryllium windows was studied using MCNP 4C2 Monte Carlo code. Radiation shielding was also studied using the Monte Carlo code for different thickness of lead as lining material. The computational study provides a means to optimize the design and performance of the proof-of-principle device, which has been constructed and is currently under testing and experimentation.

Electron trajectories and their distribution on the target were completed for three different configurations and five takeoff angles. The configuration of filament acting as the cathode at -60 kV and a floating backing plate has shown development of a hot spot at the center of the target for all takeoff angles indicating that a group of electrons are focused on the target at its center. The configuration of the backing plate is at –60kV and filament is biased by –12V has shown a more uniform distribution, however, there was a loss of electron population and many electrons fly away from the target as a result of diverging electric field between the filament assembly and the target. The configuration of both filament and backing plate both at –60kV has shown electrons are better focused on target, which results in less background radiation. It is determined that this configuration generates x-rays sufficient for DEI application.

Target heating was investigated using a heat conduction code. Three beam currents were selected for the simulation, 3mA, 30mA and 300mA. Radial and axial temperature profiles were obtained for each case showing that the center of the target has a peak temperature of 629^{o}K in 450 seconds for the 3mA case. For the 30mA beam current, the temperature increases to 1355^{o}K in 130 seconds, and for 300mA beam current the temperature approches1400^{o}K in only 3.4 seconds. In all cases, it is possible to operate without active cooling but within the limitation on the operation time. Active cooling would allow for longer operation times at higher beam currents.

The MCNP code has been used to calculate x-ray flux and shielding requirement. Two window materials were investigated, aluminum and beryllium. The K-shell characteristic x-rays $K_{\alpha1}$, $K_{\alpha2}$ and $K_{\beta1}$ have been investigated for each window material. Simulation results for aluminum window have shown that the x-ray flux decreases with increased window thickness. To achieve an x-ray flux ~10^{12} ph/cm^2/sec, the beam current must be 4A for 0.1mm aluminum window, 2A for a 0.05 mm thickness and 1.5A for a 0.01mm thickness. For beryllium window, the results show that the x-ray flux does not change when increasing the window thickness. The $K\alpha1$ x-ray flux for a beam current of 30mA with 0.01mm Aluminum window is 2.23×10^8 ph/mm^2/sec., which is four orders of magnitude less than synchrotron radiation, however, area magnification for an industrial system could provide the x-ray intensity required for DEI applications. An industrial scale device is assumed to operate with a 3A beam current and a target area of $100cm^2$, thus an x-ray flux of ~ 10^{11} ph/mm^2/sec will be reached and would be comparable to that of a synchrotron source. The use of a beryllium window would allow for higher flux at lower beam currents, with the advantage of having a thicker window over a thin aluminum one.

Radiation shielding calculations have shown that using a 0.2mm lead lining would only produce a radiation exposure of 1 mR/hr. Increasing the thickness of lead to 0.4cm reduces the radiation exposure to less than 10^{-5} mR/hr.

Future work

- Benchmark proof-of-principle device to computational results.
- Optimize design features and operational parameters.
- Conduct thermal management studies with active cooling.
- Extend computational studies to industrial scale device.

References

[1] Chapman D, Thomlinson W, Johnston RE, et al. Diffraction enhanced x-ray imaging. Phys. Med. Bio. 42:2015-2025., 1997.

[2] Chapman D, Thomlinson W, Arfelli F, et al. Mammography Imaging Studies using a Laue Analyzer Crystal. Rev. Sci. Instrum. 67(9):CD-ROM, 1996.

[3] Bushberg JT, Seibert JA, Leidholdt EM, Boone JM. The Essential Physics of Medical Imaging, Williams and Wilkins,1994.

[4] A Taibi et al, Dual-energy imaging in full-field digital mammography: a phantom study. Phys. Med. Bio. 48 (2003) 1945-1956

[5] R Thomas et al, Handbook of computed tomography x-ray spectra, U.S Department of health and human services, Public health service, Food and drug administration. HHS publication (FDA) 81-8162, (1981) 11.

[6] Pisano ED, Johnston RE, Chapman D, Geradts J, Iacocca MV, Livasy CA, Washburn DB, Sayers DE, Zhong Z, Kiss MZ, Thomlinson WC. Human Breast Cancer Specimens: Diffraction-enhanced Imaging with Histologic Correlation - Improved Conspicuity of Lesion Detail Compared with Digital Radiography. Radiology 414(3); 895-901, 2000A

[7] Zachariasen WH. X-ray interference in real crystals. In: Theory of x-ray diffraction in crystals. Wiley, New York, NY, 1955.

[8] Suortti P et al, Medical applications of synchrotron radiation, Phys. Med.Biol. 48 (2003) R1-R35.

[9] Zhong Z., Thomlinson W., Chapman D. , Sayers D. Implementation of Diffraction Enhanced Imaging at the NSLS and APS. Nucl. Instrum. Meth. In Phys. Res. A447:556-568, 2000.

[10] Pisano ED, Chapman D, Sayers D, Verghese K, Doster JM, Bourham MA, Zhong Z, Johnson RE, Cole E, Zheng Y and Yaffe M., Design of a Clinical Diffraction Enhanced Imaging Unit for Breast Imaging, 16th Annual Radiology Research Symposium, University of North Carolina at Chapel Hill, March 31, 2001.

[11] Pisano ED, Chapman D, Sayers D, Verghese K, Doster JM, Bourham MA, Zhong Z, Johnson RE, Cole E, Zheng Y and Yaffe M., Diffraction Enhanced Imaging (DEI) of Human Breast Cancer Specimens, 16th Annual Radiology Research Symposium, University of North Carolina at Chapel Hill, March 31, 2001.

[12] David A. Dahl, Idaho National Engineering and Environmental Laboratory, SIMION 3D version 7.0 User's Manual, 2000

[13] Francis F. Chen, Introduction to plasma physics and controlled fusion. 2nd ed, New York, Plenum Press, 1984.

[14] Joseph Selman, The fundamentals of imaging physics and radiobiology, Chares C Thomas Publisher, 2000.

[15] Frank P. Incropera, Introduction to heat transfer. 2nd ed, john Wiley & Sons, Inc.

[16] John R. Lamarsh, Introduction to nuclear engineering 3rd ed, Prentice Hall, 2001.

[17] ICRU, Average energy required to produce an ion pair, Report 31, International commission on Radiation Units and Measurement, Washington, D.C, 1979.

[18] Faw, Richard E. Radiological assessment: sources and doses, American Nuclear Society, Illinois USA, 1999.

[19] Briesmeister J(ed.). MCNPTM - A General Monte Carlo N-Particle Transport Code, Report LA-12625-M, Los Alamos National Laboratory, 1997.

[20] Halbleib JA, Kensek PR, Mehlhorn TA, Valdez GD, Seltzer SM, Berger MJ, ITS Version 3.0: The integrated TIGER Series of Coupled Electron/Photon Monte Carlo Transport Codes, SAND91-1634, Sandia National Laboratories, Albuquerque, NM, 1991.

[21] Halbleib J. The Integrated TIGER System in Monte Carlo Transport of Electrons and Photons, Plenum Press, New York, 1988.

[22] Z wang, Low energy electron beam accelerator design for surface sterilization of aseptic food packaging materials, North Carolina State University, Raleigh, 1994.

[23] CRC Handbook of Chemistry and Physics 84th ed, 2003-2004, CRC Press LLC.

[24] Paul M. Fishbane et al, Physics for scientist and engineers 2nd ed. Prentice hall, Upper saddle river, New Jersey, 1996.

[25] ICRU, *Tissue Substitutes in Radiation Dosimetry and Measurement,* Report 44 of the International Commission on Radiation Units and Measurements, Bethesda, MD, 1989.

Appendix I

SIMION 3D geometry code

```
PA_Define(56,71,71,planar,non-mirrored)

Locate(39,35,31,1,110,0,0)                    ;target code_20 degree angle
{
        Electrode(1)
        {
        Fill
                {
                within
                {
                        cylinder(0,0,0,18,18,10)
                        }
                }
        }
}

Locate(4,35,35,1,90,0,0)                      ;backing plate
{
        Electrode(2)
        {
                Fill
                {
                        within
                        {
                                cylinder(0,0,0,16,16,4)
                        }
                        notin
                        {
                                cylinder(0,0,0,15,15,3)
                        }
                }
        }
}

Locate(3,35,35,1,90,0,0)
{
        Electrode(3)                          ; Filament # 3
        {
                Fill
                {
                        within
```

```
                {
                        cylinder(0,0,0,12.0625,12.0625,1)
                }
                notin
                {
                        cylinder(0,0,0,11.0625,11.0625,1)
                }
        }
    }

    Electrode(4)                                ; Filament # 2
    {
        Fill
        {
                within
                {
                        cylinder(0,0,0,8.2067,8.2067,1)
                }
                notin
                {
                        cylinder(0,0,0,7.2067,7.2067,1)
                }
        }
    }

    Electrode(5)                                ; Filament # 1
    {
        Fill
        {
                within
                {
                        cylinder(0,0,0,4.45,4.45,1)
                }
                notin
                {
                        cylinder(0,0,0,3.45,3.45,1)
                }
        }
    }
}
```

Appendix II

MCNP code

Option 1 Al window 0.1 cm

```
C cell card
1 1 -8.92 -1 10 -11
2 2 -10.208 (1:-10:11) -1 9 -10
3 3 -7.874 (1:-9:11) -4 -5 6
4 0 -2 8 -12 #1 #2 #3
5 3 -7.874 (2:-8:12) -3 8 -12
6 3 -7.874 (3:-8:12) -17 3 -12 19
7 3 -7.874 (17:-3:12:-19) -17 12 -13
8 3 -7.874 (3:-8:12) -17 3 8 -18
9 4 -2.7 (17:-3:-8:18) -17 7 -8 $ Al window
10 5 -0.00129 -14 15 -16 #1 #2 #3 #4 #5 #6 #7 #8 #9
11 0 (14:-15:16)

C surface card
1 1 cz 1.74625
2 cz 7.62
3 cz 7.9248
4 cy 1.5875
5 py -2.5
6 py -5.4
7 pz -16.7688 $window thickness
8 pz -16.6688 $with surface 7
9 1 pz -.1
10 1 pz 0
11 1 pz 5.715 $target length
12 pz 16.6688
13 pz 18.8913 $half inch
14 cz 12
15 pz -20
16 pz 20
17 cz 10.16
18 pz -14.4463
19 pz 14.4463

mode p e
imp:p 1 1 1 1 1 1 1 1 1 1 0
imp:e 1 1 1 1 1 1 1 1 1 0 0
sdef erg=0.06 sur=5 pos=0 -2.5 0 rad=d1 par=3 dir=1 ara=7.9173 vec=0 1 0
si1 1.5875
```

```
sp1 -21 1
m1 29000.02p 1
m2 42000.02p 1
m3 26000.02p 1
m4 13000.02p 1
m5 7000.02p 0.78 8000.02p 0.22
tr1 0 0 0 1 0 0 0 .3826 -.92388 0 .92388 .3826 1
e0 1.0e-5 9999I 0.1 $Ka2 0.01737 Ka1 0.01748 Kb1 0.01961
f2:p 15 $surface flux
nps 100000000
prdmp  100000000 100000000 1 1
print
```

Figure A- 1 MCNP simulation view